INVESTIGATION OF ULTRASONIC PRESSURE DISTRIBUTION IN A SONOREACTOR AND A WASHING TANK BY FEM SIMULATION

BY

YANFANG LI

THESIS

Submitted in partial fulfillment of the requirements
for the degree of Master of Science in Agricultural Engineering
in the Graduate College of the
University of Illinois at Urbana-Champaign, 2011

Urbana, Illinois

Adviser:

Associate Professor Hao Feng

ABSTRACT

The aim of this study is to investigate the ultrasonic pressure distribution in a sonoreactor and an ultrasonic washing tank by finite element method (FEM) by taking into account the coupling effect between the acoustic pressure in water and the mechanical vibration of the solid structure.

To examine the ultrasound intensity distribution in a sonoreactor with a fixed volume of water, the ultrasonic pressure distribution at different L values, which was the distance between the tip of the ultrasound probe and the bottom of the reactor inner wall, was simulated. The ultrasound intensity distribution was then calculated based on the acoustic pressure distribution obtained from the FEM simulation. The validity of the computer simulation was evaluated by comparing the ultrasound intensity distributions in the sonoreactor at two different L values with the result of a microbial inactivation test conducted in the same sonoreactor for each L value when treated by mano-thermo-sonication in a batch operation.

The acoustic pressure field between two transducer boxes in a custom-made ultrasound-assisted washing tank was simulated, which was then compared with the result of an erosion test with aluminum foils. A relatively good agreement was achieved between the FEM simulation and the pitting patterns formed on the aluminum foils caused by cavitation activities. With the current design of the ultrasound-assisted washing tank, both the simulation and erosion test showed that the ultrasound field distribution between two transducer boxes in the washing tank was relatively uniform.

ACKNOWLEDGMENTS

I would like to express my appreciation to all the people who helped me with this research project. I sincerely thank my adviser, Professor Hao Feng, who guided me in this project, encouraged me all along, and helped me in the preparation of this thesis. I also want to thank my committee members, Professor Mary-Grace Danao and Professor Steven R. Eckhoff, for their valuable advice and suggestions on my research and thesis. Many thanks go to my labmates Dr. Bin Zhou, Dr. Hyoungill Lee, and Sindy Palma for their assistance during the course of the experiments. I would also like to thank USDA for providing financial support through a special research grant (MAFMA) and Food Technology Noord-Oost Nederland for providing funding to support this project. Special thanks go to my family for their understanding, support, and encouragement.

TABLE OF CONTENTS

LIST OF SYMBOLS

A	Coupling Matrix
C	Wave Velocity at Bubble Wall
c	Instant Wave Velocity
c_0	Constant Wave Velocity
$\tilde{c}$	Complex Wave Velocity
d	Displacement Vector of Beam
d_p	Pressure Transmission Coefficient
d_v	Velocity Transmission Coefficient
d_I	Energy Transmission Coefficient
F	Force
f	Frequency
f_n	Number Density of Bubbles
I	Sound Intensity
I_0	Sound Intensity at the Sound Source
K	Bulk Modulus
K_{ad}	Adiabatic Linear Bulk Modulus
K_f	Bulk Modulus of Fluid
k	Wave Number
$\tilde{k}$	Complex Wave Number
P	Pressure
p_0	Static pressure
p	Excessive Pressure
p_c	Cavitation Threshold
∇p	Pressure Gradient

R	Instant Bubble Radius
R_0	Equilibrium Bubble Radius
r	Radius
$\hat{S}$	Stiffness Matrix of Fluid
S	Stiffness Matrix of Beam
s	Condensity
T	Temperature
t	Time
U	Displacement Amplitude
$\tilde{u}$	Complex Displacement
u	Displacement
V_o	Volume
$\dot{V}_o$	Volume Displacement
$\ddot{V}_o$	Volume Acceleration
V	Velocity
v	Relative Velocity of particles
v_0	Velocity of Steady Flow
W	Energy
W_{pot}	Potential Energy
W_{kin}	Kinetic Energy
w	Instantaneous Energy Density
$\overline{w}$	Average Energy Density
X	Spatial Position
xx	Input Acoustic Signal
x	Coordinate in x direction
y	Coordinate in y direction
z	Coordinate in z direction

z_0	Specific Characteristic Impedance
z_1	Acoustic Impedance of Medium 1
z_2	Acoustic Impedance of Medium 2
$\tilde{z}$	Specific Impedance
z_i	Imaginary Part of Specific Impedance
$\tilde{Z}$	Total Impedance
φ	Velocity Potential
ψ	Amplitude of a Monochromatic Wave
α_0	Attenuation Coefficient
β	Bubble Volume Fraction
β_0	Initial Phase
ω	Angular Frequency
ω_0	Resonance Angular Frequency
η	Bulk Viscosity Coefficient
μ	Shear Viscosity Coefficient
λ	Wave Length
γ	Volumetric Drag
ρ	Density of the Medium
ρ_0	Density of the Unperturbed Medium
$\Delta\rho$	Density Difference
ρ_p	Pressure Reflection Coefficient
ρ_v	Velocity Reflection Coefficient
ρ_I	Energy Reflection Coefficient

CHAPTER 1 INTRODUCTION

Fruits and vegetables are an essential part of human diet. In recent years, the global fruit and vegetable consumption has increased continuously (Venkitanarayanan et al., 2002). While the presence of spoilage bacteria, yeasts, molds and pathogens on fresh produce has been recognized nearly a century ago (Beuchat, 1998), fruits and vegetables are traditionally considered microbiologically safer than meat, poultry, eggs, milk and seafood. Most fresh raw fruits and vegetables are processed slightly to increase the convenience and value of the product before going into commercial distribution (De Roever, 1998). Some fresh, raw fruits and vegetables are minimally processed refrigerated and then sold to consumers in a ready-to-eat form (Wiley, 1994).

However, outbreaks of human pathogen infections associated with the consumption of fruits, vegetables, and unpasteurized fruit juices or ciders have become more frequent over the past two decades (Parish, 1997; De Roever, 1998; Olsen et al., 2000; Lynch et al., 2006; CDC, 2009), which give rise to public health concerns about the microbial safety of fresh produce. According to the Center for Science in the Public Interest information, the number of foodborne illness outbreaks in produce have doubled between 1998 and 2004, with 44 outbreaks in 1994 (CDC, 2006) and more than 100 outbreaks in 2004 (AFF, 2010). Table 1.1 summarizes selected outbreaks of fresh produce in the U.S. in recent years.

Table 1.1. Recent outbreaks of foodborne illness associated with fresh produce in the United States*

Year	Vehicles known	Cases	Death
2006	Tomato, spinach	382	3
2007	Basil, baby corn, alfalfa sprouts	271	
2008	Jalapeno peppers, serrano pepper, tomato	1442	2
2009	Alfalfa sprout	235	
2010	Alfalfa sprout, romaine lettuce	260	

*Based on information provided by CDC in 2006, 2007, 2008, 2009, and 2010.

Unpasteurized fruit juices when contaminated by pathogenic organisms can also greatly endanger the lives or health of human beings. In October 1996, unpasteurized commercial apple juice resulted in three outbreaks of gastrointestinal illness, among which one outbreak of *Escherichia coli* O157:H7 infection caused illness in 66 persons and one death (CDC, 1997). To enhance the microbial safety of fresh fruits, vegetables and fruit juices, improved methods to inactivate foodborne pathogens are of great importance.

1.1 Traditional Fresh Produce Decontamination Methods

1.1.1 Traditional Wash and Decontamination Methods

Fruits and vegetables are prone to contamination of microorganisms capable of causing human diseases while on the plant, or during harvesting, transport, processing, marketing or in the home (Beuchat, 1998). In pre-harvest practices, specific measures must be taken to prevent contamination of produce by human pathogens from different sources. In post-harvest handling, normally a decontamination technology is used to significantly reduce the number of microorganisms on the product. Currently, a surface decontamination operation is employed in fresh produce production to reduce the population of microorganisms and minimize the food safety risk, while for liquid foods, such as juices, a pasteurization with thermal energy is often used to achieve a 5 log cycles reduction in the number of pathogenic organisms.

Most fresh produce is subjected to a batch tank or water spray wash after harvest to remove soil and debris, lower produce's temperature, and limit the physiological changes. This first step wash also reduces the microbial load on the surface of the fresh produce, which impacts the produce quality, shelf-life, and safety (Herdt and Feng, 2009). It is common for processors to recycle the water to lower the production cost. This reuse of wash water enhances the risk of cross-contamination, which facilitates the transmission of pathogens or other bacteria from the contaminated produce to water and then to uncontaminated produce. Therefore proper sanitization of the wash water is of great importance. In practice there are

many kinds of sanitizers used in industry, such as chlorine, chlorine dioxide, acidified sodium chlorite, peroxyacetic acid, hydrogen peroxide, and bromine (Herdt and Feng, 2009; Beuchat, 1998). The efficacy of these sanitizers depends on many factors such as washing time, sanitizer concentration, temperature, the pH of the solution, sanitizer flow hydrodynamics, organic loading, microbial type, level and attachment, produce surface properties and so on (Herdt and Feng, 2009). The sanitation wash with a concentration allowed by FDA without compromising the quality of the produce can only reduce the number of pathogenic and spoilage microorganisms by 10 to 100-fold, or 1 to 2 log cycles (Beuchat, 1998; Allende et al. 2006).

For fruit juices, pasteurization has long been used for microbial inactivation as well as for extending shelf life (Lee et al., 2009a). Pasteurization refers to a rapidly heating and cooling procedure of liquid foods to achieve a 5 log cycles reduction in the number of a target pathogenic microorganism. Bacteria, yeast, and mold causing spoilage will also be inactivated in a pasteurization process. Although the typical pasteurization conditions for microbial stability are 85^{o}C for 15–30 seconds, a higher temperature, typically 95^{o}C for a few seconds is necessary to inactivate pectic enzymes (Ashurst, 2007).

1.1.2 Deficiencies of Traditional Wash and Decontamination Methods

The efficacy of a traditional treatment of fresh produce is not always stable. The efficacy varies greatly with the nature of the microorganisms, the chemical and physical characteristics of inner and surface tissues of fruit and vegetable, and contact time and temperature (Beuchat, 1998). The same disinfectant solution used for the same pathogen removal may not produce the same result when used on different produce.

The currently-used sanitizers are unable to eliminate pathogenic microorganisms on fresh produce, and their efficacy is far from satisfactory. For example, treatment of apples with water containing chlorine or a commercial sanitizer approved for fruits and vegetables generally only reduces bacterial pathogens by less than 2- to 3- log CFU per gram produce specimen in laboratory wash tests (FDA, 1998a; Sapers, 1999). Water containing 50 to 100 mg/l free chlorine only reduces microbial population on produce surfaces to 1- to 2-log CFU/g (Sapers,

1998). While the U.S. Food and Drug Administration (FDA) proposed that treatments of fruits and vegetables should be able to reduce the pathogen loads by a minimum of 5 log cycles (FDA, 1998b), there is no available sanitation method that can achieve the 5 log reduction without compromising the quality of the produce.

Furthermore, the efficacy of a sanitizer is often minimized when the pathogens are attached to produce surfaces or entrapped in plant tissues. The reason lies in the fact that:

1) Biofilms could form on produce which provide microenvironments where human pathogens could grow and be protected against chemical sanitizers (Carmichael et al., 1999).

2) Human pathogens can enter vegetable or fruit tissues and behave as endophytes, in such case surface sanitation would not be effective for their removal (Beuchat, 2004).

3) For pathogens infiltrated into protected surface and subsurface structures and tissues of fruits and vegetables, an aqueous chemical solution can hardly reach them (Beuchat, 2004).

In addition, as describe by Wiley (1994), fresh produce undergoes many kinds of nutrition and sensory loss during the wash, cut, and storage phases.

Another issue is the sanitizer residues on fresh produce. A high level of residues is a serious threat to the health of human beings. The maximum residue limits set by many countries are becoming more and more strict (Pan et al., 2008). This fact, accompanied with increased consumer demand for new methods of food processing that have minimal impacts on nutritional content and overall food quality, makes it necessary to find safer methods to remove bacteria on fresh fruits and vegetables.

1.1.3 Deficiencies of Pasteurization

For juice products, traditional thermal pasteurization treatments reduce the sensory and nutrition values (Piyasena et al., 2003; Lee et al., 2009b), and thus degrade product quality. Besides, traditional thermal pasteurization treatments are less energy efficient and the treatment may be less uniform, especially for small scale production (Piyasena et al., 2003). Researchers have been looking for alternative methods to thermal pasteurization in liquid food processing. Several alternative physical methods have been proposed and tested over the years,

including ultrasound, high pressure processing (HPP), high-intensity electric field pulses, light pulses, oscillating magnetic fields, ionizing radiation, gamma irradiation, and ultraviolet radiation (Butz and Tauscher, 2002; Allende et al., 2006; Gil et al., 2009). Among all the innovative methods, the ultrasound technology is unique because it can be used for both surface decontamination of fresh produce (Allende et al., 2006; Zhou et al., 2009) and volumetric treatment of juice products (Ugart- Romero et al., 2006; Lee et al., 2009a).

1.2 Ultrasound

1.2.1 Ultrasonic Waves

Sound is a waveform resulting from local density variations (compression and rarefaction) in an elastic medium. It can be transmitted through any elastic substance, solid, liquid or gas (Leighton, 1994; Lorimer and Mason, 1987).

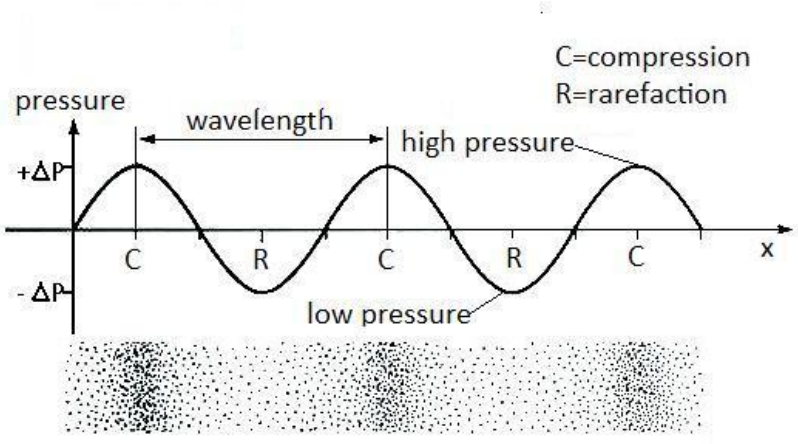

Figure 1.1. Acoustic waveform

The source of a sound wave is usually a vibrating body, which transmits its mechanic vibration to the molecules of the elastic medium around it. The molecules then oscillate around their equilibrium positions and transmit the oscillation to adjacent particles (Lorimer and Mason, 1987). There are alternative compressions and rarefactions of the medium particles (Figure 1.1), which cause the propagation of sound in the medium (Povey and Mason, 1998).

In a liquid or gas, acoustic waves are longitudinal waves with medium particles' displacement parallel to the direction of motion of the wave. While in a solid, acoustic waves could be longitudinal or transverse waves since the solid possesses shear elasticity which can support tangential stresses (Lorimer and Mason, 1987). The frequencies of acoustic waves which human beings can hear range from 20 Hz to 20 kHz. Ultrasound is defined as sound with a frequency greater than 20 kHz (Leighton, 1994; Butz and Tauscher, 2002), as shown in Figure1.2.

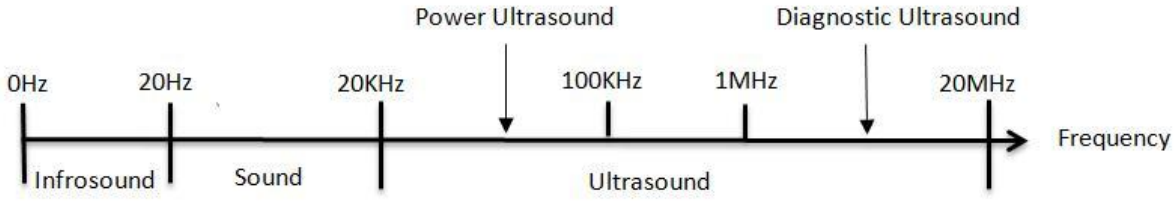

Figure 1.2. Acoustic frequency spectrum

The ultrasound energy transmitted to a medium can be expressed by ultrasound power (W), ultrasound intensity (W/cm^2), acoustic power density (W/cm^3), and cavitational intensity. Recently, the acoustic power density has been widely used to measure the ultrasonic power level (O'Donnel et al., 2010).

1.2.2 Ultrasound Systems

An ultrasound system usually consists of three essential parts: a generator that converts electricity at 50 or 60 Hz into high frequency alternating current, a transducer that converts the high-frequency alternating current into mechanical vibrations, and a delivery system that amplifies and conveys the vibration into a food processing system, such as an ultrasonic cleaning tank and the horn of an ultrasonic probe system (Feng and Yang, 2006).

Figure 1.3. Ultrasound system

For power ultrasound applications, there are mainly two types of transducers, magnetostrictive and piezoelectric, both driven by electricity (Feng and Yang, 2006; Mason and Lorimer, 2002).

Magnetostrictive transducers utilize the phenomenon of magnetostriction to generate power ultrasound. Magnetostriction refers to the effect found in some materials such as nickel which changes their dimensions when placed in a magnetic field and returns to normal dimensions when the field is removed. Magnetostrictive transducers consist of a core of a large number of nickel laminations which are arranged in parallel with one edge of each lamination attached to the surface to be vibrated, and a copper solenoid which can generate a series of short pulse magnetic field. When alternate electric current flows through the solenoid, the magnetostrictive core contracts or elongates, thereby introducing acoustic vibration. The frequency range of this type of transducer is limited to below 100k Hz, while the electrical efficiency of the system is only about 60% due to heat generated during the process. (Feng and Yang, 2006; Mason and Lorimer, 2002; Povey and Mason, 1998) .

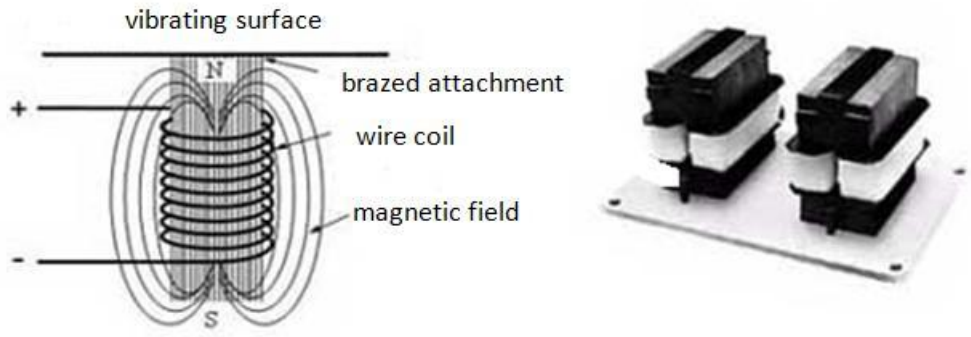

Figure 1.4. Magnetostrictive transducer (CTG, 2009)

Piezoelectric transducers utilize the piezoelectric effect to transform electricity to mechanical vibration (Figure 1.5). The essential part of a piezoelectric transducer is a piezoelectric element (ceramic disk) made of barium titanate, lead metaniobate, or the mixed crystal lead zirconate titanate, sandwiched between two metal blocks that serve to protect the crystalline material and to prevent it from overheating. Two electrodes are connected to the two sides of the ceramic assembly respectively. On applying rapidly alternate electric current to the piezoelectric ceramic, fluctuation in its dimensions will be generated. This physical displacement results in ultrasound waves. The frequency range of piezoelectric transducers is very wide while the energy efficiency of the system is above 70% (Feng and Yang, 2006).

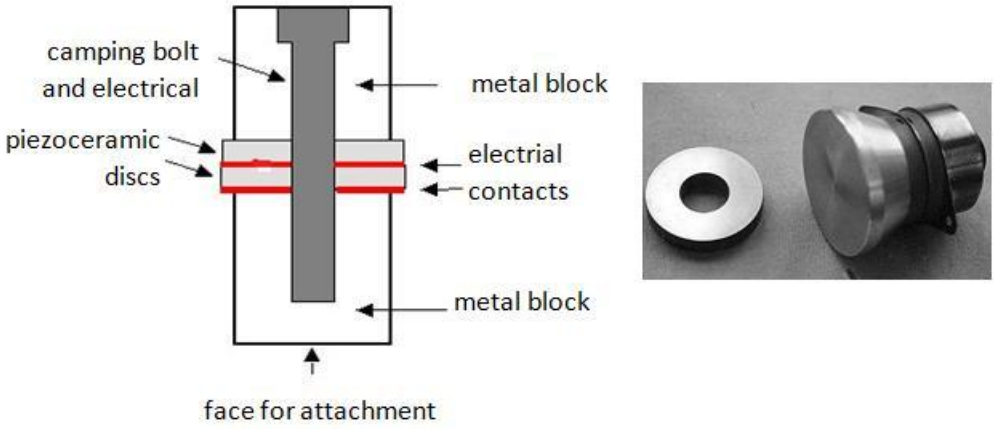

Figure 1.5. Piezoelectric transducer (SCCU, 2007)

1.2.3 Application of Power Ultrasound in Surface Cleaning and Decontamination

Nowadays, ultrasound is widely used in medical, industrial and chemistry applications. Though the applications of ultrasound are diverse, it can generally be divided into two categories according to the frequency used and the acoustic energy involved: diagnostic ultrasound and power ultrasound. Diagnostic ultrasound operates at 1 to 10 MHz with a sound intensity of 0.1 to 1 W/cm^2, while power ultrasound operates at 20 to 100 kHz with an intensity of 10 to 1000 W/cm^2 (Feng and Yang, 2006; Piyasena et al., 2003; Povey and Mason, 1998).

The applications of diagnostic ultrasound include: ultrasound imaging, medical scanning, and nondestructive detection (Mason, 2003). The applications of power ultrasound include: surfaces cleaning and decontamination, medical treatment, biological cell disruption, ultrasonic cutting, homogenization, extraction, drying, deforming, ultrasonic plastics soldering, metal welding, ultrasonic machining, and ultrasonic therapy (Mason, 2003; Mason and Lorimer, 2002; Lin and Zhang, 2000; Suslick, 1986).

Power ultrasound has long been used for solid surface cleaning and decontamination in laboratories. It is used to remove dirt and bacteria from solid surfaces used in medical, surgical and dental industries. Objects that can be cleaned by ultrasound range from large crates used for food packaging and transportation to small, delicate surgical tools such as endoscopes (Mason and Lorimer, 2002). Ultrasonic cleaning has a particular advantage over traditional cleaning methods, that is, it can reach small crevices that are difficult or even not able to access when using conventional cleaning methods.

1.2.4 The Mechanism of Ultrasonic Cleaning and Decontamination

The mode of action in ultrasonic solid surface cleaning is normally attributed to acoustic cavitation. When a cavitation bubble implodes near a solid surface, a powerful water jet is produced which can dislodge dirt and bacteria (Mason and Lorimer, 2002) (Figure 1.6). However, the water jet cannot explain all. Besides the mechanical removal of attached or entrapped microbes, inactivation of foodborne pathogens and spoilage micro-organisms or enzymes by sonication is mainly due to disruption of cellular structure, cell lysis under intracellular cavitation, and sonochemical production of free radicals due to pyrolysis of water (O'Donnel et al., 2010; Kim et al., 2007; Gogate et al., 2003; Butz and Tauscher, 2002; Fellows, 2000).

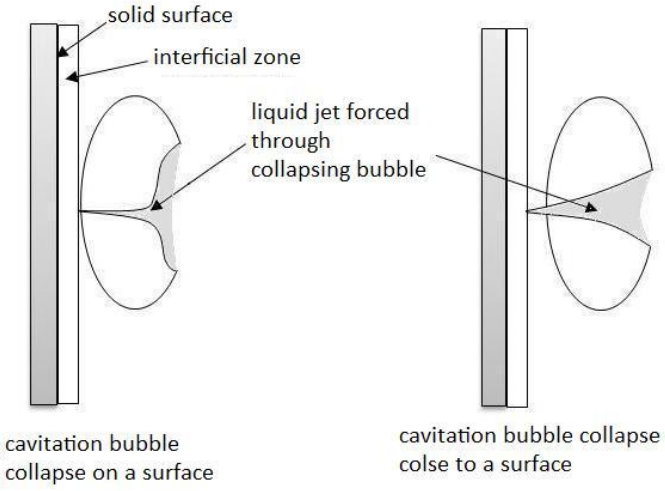

Figure 1.6. Effect of sonication in a liquid near a solid surface (Mason and Lorimer, 2002)

Cavitation refers to the formation, growth, and implosion of gas- or vapor-filled cavities in a liquid which takes place in an extremely small interval of time (milliseconds) with large amounts of energy released (Feng and Yang, 2006; Leighton, 1994). In pure water, cavities are formed when the tensile force produced by the negative pressure in the rarefaction cycle of the sound wave is greater than the tensile strength between water molecules (Shutilov, 1988; Suslick, 1986).

It is the formation and behavior of cavitating bubbles in an acoustic field that induces the majority of the acoustic effects (Soria and Villamiel, 2010; Kim et al., 2007; Dähnke and Keil, 1998; Save et al., 1997; Flint and Suslick, 1991). During cavitation, the nearly adiabatic compression of a gas babble generates enormous heat, resulting in a local temperature as high as 6,000 Kelvin in water and other fluids, while the implosion of the babbles can induce very high localized pressure of up to 50 MPa (Kim et al., 2007; Rae et al., 2005; Leighton, 1998; Flint and Suslick, 1991). The rapidly changed high pressure results directly in the disruption of cellular structure (Hunter et al., 2008). The high temperature and high pressure produced during intracellular cavitation can lead to the cell lysis, and free radicals can directly inactivate virus and microbes as a sonochemical effect of cavitation.

The research of cavitation is complex. It is relevant to the studies of heat transport, liquid tensile strengths, and superheating and boiling phenomena (Apfel, 1981; Rooney, 1981). The

amount of energy released by cavitation depends on the kinetics of the bubble growth and collapse of the bubbles.

1.3 Application of Ultrasound in Food Processing

1.3.1 Ultrasonic Cleaning and Decontamination for Fresh Produce

Though the lethal effect of ultrasound on microorganisms was firstly reported in 1930s (Harvey and Loomis, 1929), ultrasound as a potential microbial inactivation method was not studied until 1960s (Earnshaw et al., 1995).

Mott et al. (1998) investigated the application of ultrasound at frequencies ranging from 20 kHz to 350 kHz to remove mineralized *Proteus* biofilm. The results showed that three 30-s exposures to 20 kHz ultrasound removed 87.5% of the biofilm. Seymour et al. (2002) found that ultrasound was able to enhance the deduction of *Salmonella typhimurium* attached to iceberg lettuce by one log cycle over that of washes with only a sanitizer. The research conducted by Scouten and Beuchat (2002) showed that an ultrasound treatment in combination with chemical and heat could enhance the removal of pathogens on alfalfa seeds. Huang et al. (2006) reported more than one log cycle additional reduction of *S*. *enterica* and *E. coli* O157:H7 on apples and lettuce when ultrasound was applied in chlorine dioxide treatments. Berrang et al. (2008) reported that a 60s ultrasonication improved the performance of both quaternary ammonium- and chlorine-based chemicals in inactivating planktonic cells in the inner wall surface of chloride drain pipes by log 3.1 and 2.9 CFU/cm^2, respectively. Ultrasound can also enhance the reduction of *E. coli* on spinach by one log cycle over that of washes with sanitizer alone with reduced processing time (Zhou et al., 2009).

The mechanical cleaning action appears to remove microbes attached to or entrapped in the surface of fresh produce, rendering the pathogens more susceptible to sanitizer. Besides, the energy released by cavitation may disrupt cellular structure of microbes suspending in water and on the surface of produce.

1.3.2 Ultrasound Treatment of Liquid Foods

For liquid food such as fruit juices, ultrasound in combination with other treatments is able to meet the FDA's mandatory 5 log reduction of food borne pathogens in fruit juices. Rodgers and Ryser (2004) reported an accumulated 5-log deduction of *E. coli* O157:H7 and *Listeria monocytogenes* in apple cider with the use of copper ion water, sodium hypochlorite and sonication. Baumann et al. (2005) indicated that the use of ultrasound in combination with a mild treatment condition could achieve a 5-log reduction of *L. monocytogenes* in apple cider. Ugarte-Romero and coworkers (2006) demonstrated that ultrasound in combination with a mild thermal treatment resulted in a 5-log reduction of *E. coli* in apple cider. In the experiments conducted by Lee et al. (2009b), it was found that ultrasound in combination with mild thermal and pressure treatment can reduce *E. coli* k12 population by 5-log in tryptic soy broth in less than 30 seconds.

The inactivation of pathogens and spoilage microorganisms in liquid foods is mainly due to disruption of cellular structure and cell lysis under intracellular cavitation. If the treatment conditions are carefully controlled, ultrasonic processing of fruit juices may have minimal effects on the quality of fruit juices, such as orange juice, guava juice and strawberry juice. It can also inactivate harmful enzymes responsible for deterioration of fruit and vegetable juice and various enzymes pertinent to milk quality (O'Donnell et al., 2010).

CHAPTER 2 THEORETICAL BACKGROUND

2.1 Wave Equation

Most acoustic waves exist in four dimensions of space and time. The acoustic wave equations are derived via thermodynamic, kinematic and dynamic relations (Shutilov, 1988; Fahy, 2001).

In the derivation of wave equations, there are three main assumptions (Shutilov, 1988). The first is that the medium in which the wave propagates is an ideal liquid, where an ideal liquid refers to a medium exhibiting only volume elasticity and no elasticity of shape and viscosity. Secondly, the oscillation amplitude of the acoustic wave is infinitesimal, usually less than one hundred microns. The third assumption is that the propagation of ultrasonic waves is an adiabatic process. When compression waves propagate in a medium, the temperature oscillates. Since the compression process is extremely short, the losses of heat due to the finite thermal conductivity of the medium can be neglected.

2.1.1 3-D Waves

To describe the propagation of ultrasound in a liquid, the medium density ρ, the pressure P, and the displacement of particles from their equilibrium position u, and the displacement rate $v = du/dt$ are taken as the basic acoustic parameters (Shutilov, 1988). Here, a particle is a fictitious entity that refers to a small region surrounding the point of interest in the medium, which allows convenient expressions of the average position, velocity and acceleration vectors of the molecules in that region (Fahy, 2001).

Each parameter named above consists of a constant component and a finite increment, which depends on the coordinates and time thus: $P = p_0 + p(x, y, z, t)$, $\rho = \rho_0 + \Delta\rho(x, y, z, t)$, and $V = v_0 + v(x, y, z, t)$, where p_0 is the static pressure; ρ_0 is the density of the unperturbed

medium; and v_0 is the velocity of steady flow, which in our case was zero, therefore, $V = v(x, y, z, t)$.

The equation of motion is

(2-1) $$-\nabla p = \rho \frac{dv}{dt} = \rho\left(\frac{\partial v}{\partial t} + (v\bullet\nabla)v\right).$$

The equation of continuity is

(2-2) $$-\frac{1}{\rho}\frac{d\rho}{dt} = \nabla\bullet v.$$

The adiabatic equation of state for liquids is

(2-3) $$p = K_{ad} s,$$

where $K_{ad} = \rho_0 \left(dp / d\rho\right)_{\rho=\rho_0}^{ad}$ is the adiabatic linear bulk modulus. $s = \Delta\rho / \rho_0$ is called condensity.

By introducing a scalar function $\varphi(x, y, z, t)$, which is called velocity potential, and linearizing equation (2-1), (2-2) and (2-3), we get the wave equation in the following form

(2-4) $$\Delta\varphi = \frac{1}{c_0^2}\frac{\partial^2\varphi}{\partial t^2},$$

where $v = -\nabla\varphi$, $\Delta\varphi = \frac{\partial^2\varphi}{\partial x^2} + \frac{\partial^2\varphi}{\partial y^2} + \frac{\partial^2\varphi}{\partial z^2}$, $c_0^2 = \left(\frac{dp}{d\rho}\right)_{\rho=\rho_0} = K_{ad} / \rho_0$, c_0 is called the wave velocity.

2.1.2 Plane Waves

If the velocity potential and all other acoustic parameters depend on only one Cartesian coordinate, then the wave is a one-dimensional plane wave. For plane waves, each acoustic quantity is uniform on any plane perpendicular to the direction of wave propagation. Plane acoustic waves are realized only at ultrasonic frequencies. The equation of a plane wave is:

(2-5) $$\frac{\partial^2\varphi}{\partial x^2} = \frac{1}{c_0^2}\frac{\partial^2\varphi}{\partial t^2}.$$

2.1.3 Monochromatic Plane Waves

A monochromatic plane wave refers to a plane wave propagating from a source oscillating harmonically with frequency ω. The velocity potential of a monochromatic wave can be represented as:

(2-6) $$\varphi(x,t) = \psi(x)\sin(\omega t + \beta_0)$$

where β_0 is an arbitrary initial phase of the oscillation.

Substituting equation (2-6) into the wave equation (2-5), we can get a forward wave:

(2-7) $$\varphi(x,t) = \varphi_{\max}\sin(\omega t - kx),$$

(2-8) $$p = \rho_0 \frac{\partial \varphi}{\partial t} = \rho_0 \omega \varphi_{\max}\cos(\omega t - kx) = p_{\max}\cos(\omega t - kx),$$

(2-9) $$v = -\partial\varphi / \partial x = k\varphi_{\max}\cos(\omega t - kx) = v_{\max}\cos(\omega t - kx),$$

where $k = \omega / c_0$ is the wave number.

2.2 Terminology of Sound

2.2.1 The Velocity of Sound

The quantity c_0 in the wave equation (2-4) represents the velocity with which elastic waves propagate, so c_0 is called the velocity of sound. Its magnitude is determined by equation (2-10)

(2-10) $$c_0 = \sqrt{(K_{ad} / \rho_0)}.$$

This equation is exact only for infinitesimal perturbations. However, in nonlinear elasticity media for finite-amplitude waves, only a small correction is need to the magnitude of the wave velocity. So the velocity of sound is practically constant over a very wide range of wave perturbation amplitudes. There is no need to distinguish between the velocity of sound and the velocity of ultrasound (Shutilov, 1988).

The velocity of sound in almost all liquids decreases monotonically with temperature at a considerable rate (by 2-6 $\frac{\text{m}}{\text{s•c}}$) except in water. In water, at low temperatures, the velocity of sound increases with a temperature coefficient $\frac{dc_0}{dT} \simeq 2.5 \frac{\text{m}}{\text{s•c}}$, and attains the maximum velocity of $1550\ \text{m/s}$ at 67 ^{o}C, then decreases as seen in normal liquids (Shutilov, 1988).

2.2.2 Acoustic Impedance

In physics, the definition of impedance is the ratio of a general driving force to the velocity of response (Leighton, 1998). For acoustic waves, the driving force is the acoustic pressure amplitude, and the velocity is the particles velocity in the medium. In general, the acoustic pressure and particle velocity differ in phase, so the ratio of the pressure to the particle velocity is characterized by a complex number. For this reason, $\tilde{z} = p / v = z_0 + iz_i$ is called specific acoustic impedance. Multiplication of the specific impedance by the area S on which the acoustic pressure p acts, gives the total impedance $\tilde{Z} = \tilde{z}S$. For monochromatic waves, the acoustic pressure and particle velocity have the same phase. They are related by $p = \rho_0 c_0 v$. So $z_0 \equiv \rho_0 c_0$ is called the specific characteristic impedance of the medium, which determines the magnitude of the particle velocity with fixed acoustic pressure.

2.2.3 Ultrasonic Energy Density

During the propagation of an ultrasonic wave, each particle of the medium oscillates about its equilibrium position with a velocity v, accompanied with a periodic change in density and pressure in the vicinity of the particle. Equations (2-8) and (2-9) show the pressure and velocity for monochromatic plane waves have the same phase. This means that the ultrasonic pressure forces do positive work, which, in the absence of absorption, must remain in the form of elastic oscillatory motion. So, there are two kinds of energy forms, potential energy of elastic deformation and kinetic energy, which are transmitted into the medium from the wave source.

For a volume V_0 in an unbounded monochromatic plane wave field, the potential energy equals

(2-11) $$W_{pot} = \int_0^s V_0 K s ds = \frac{1}{2} V_0 K s^2 = \frac{1}{2} \rho_0 V_0 v_{\max}^2 \sin^2(\omega t - kx).$$

The kinetic energy equals

(2-12) $$W_{kin} = \frac{1}{2} \rho_0 V_0 v^2 = \frac{1}{2} \rho_0 V_0 v_{\max}^2 \sin^2(\omega t - kx).$$

The instantaneous energy density is

(2-13) $$w = \frac{W}{V_0} = \frac{W_{kin} + W_{pot}}{V_0} = \rho_0 v_{\max}^2 \sin^2(\omega t - kx).$$

The average energy density is

(2-14) $$\bar{w} = \rho_0 v_{\max}^2 / 2.$$

2.2.4 Ultrasonic Intensity

The concept of ultrasonic intensity is defined as the energy crossing a unit surface area perpendicular to the direction of propagation of the ultrasonic wave per unit time. Since the velocity of sound waves is c_0, so the ultrasonic intensity is

(2-15) $$I = \bar{w} c_0 = \frac{1}{2} \rho_0 c_0 v_{\max}^2 = \frac{1}{2} p_{\max}^2 \frac{1}{\rho_0 c_0} = \frac{1}{2} p_{\max} v_{\max}.$$

2.3 Phenomena Associated with Wave Propagation

2.3.1 Acoustic Attenuation

As acoustic waves propagate in a medium, its intensity and amplitude decrease continuously and the waves are attenuated. This attenuation results from several mechanisms, such as divergence, scattering, and energy dissipation (absorption).

Divergence results from the simple fact of a geometric spreading of the sound wave accompanied with a decrease of the wave intensity. In this case, however, the total wave energy is not lost.

Scattering refers to the reflection of the propagating sound wave from an obstacle with appropriate dimension, which means the dimension of the obstacle must be close to or less than the sound wave length. Here, an obstacle refers to any foreign substance in the medium whose acoustic impedance differs greatly from that of the surrounding medium (Komarov et al., 2005).

Sound energy dissipation or absorption involves the transformation of part of wave energy into heat. In most fluids, ultrasonic absorption is caused primarily by viscosity which induces the internal friction (Shutilov, 1988). Sound energy dissipation is the main cause of sound intensity attenuation in most applications of ultrasound, especially in a homogeneous medium.

By introducing the viscosity coefficient of the medium η, and taking into account the fact that viscous stresses are functions of the gradient of displacement velocity of the particles of the medium, ultrasonic absorption can be calculated.

The solution for sinusoidal plane waves propagating in a viscous medium is

(2-16) $$v(x,t) = v_{\max 0} e^{-\alpha_0 x} e^{j(\omega t - kx)},$$

(2-17) $$p(x,t) = p_{\max 0} e^{-\alpha_0 x} e^{j(\omega t - kx)},$$

(2-18) $$I = I_0 e^{-2\alpha_0 x},$$

where, $\alpha_0 = 2\pi^2 f^2 \eta / (\rho_0 c_0^3)$; $f = \omega/(2\pi)$ is the frequency of the wave; and x is the distance from the wave source to the measure point in the direction of wave propagation.

2.3.2 Wave Reflection at the Boundary

At a boundary which separates two media, a wave is partially reflected, and partially transmitted into the second medium. Let a monochromatic plane wave, which propagates along the x axis, be incident normally on the boundary between two media 1 and 2 with densities ρ_1 and ρ_2, and velocity c_1 and c_2, respectively (Figure 2.1).

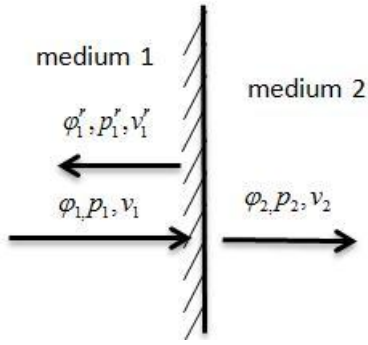

Figure 2.1. Wave reflection and transmission

In the Figure 2.1, the subscript 1 represents the incident wave, the subscript 2 represents the transmitted wave, and the superscript *r* represents the reflected wave. The ratio of reflective wave to incident wave can be described by the pressure and velocity reflection coefficients ρ_p and ρ_v, respectively.

(2-19) $$\rho_p = \frac{p_1^r}{p_1} = \frac{z_2 - z_1}{z_2 + z_1},$$

(2-20) $$\rho_v = \frac{v_1^r}{v_1} = \frac{z_1 - z_2}{z_1 + z_2}.$$

Similarly, the ratio of transmitted wave to incident wave can be described by pressure and velocity transmission coefficients d_p and d_v.

(2-21) $$d_p = \frac{p_2}{p_1} = \frac{2z_2}{z_1 + z_2}.$$

(2-22) $$d_v = \frac{v_2}{v_1} = \frac{2z_1}{z_1 + z_2}.$$

And energy reflection coefficient ρ_I and transmission coefficient d_I are given by:

(2-23) $$\rho_I = \frac{I_1^r}{I_1} = \left[\frac{z_1 - z_2}{z_1 + z_2}\right]^2.$$

(2-24) $$d_I = \frac{I_2}{I_1} = \frac{4z_1 z_2}{(z_1 + z_2)^2}.$$

Equations (2-18)—(2-23) are valid for both monochromatic and nonmonochromatic plane waves, and independent of the ultrasonic absorption in these media.

2.3.3 Standing Plane Waves

When a sound wave is incident normally on a flat boundary of the medium in which it is propagating, and if the energy absorption is neglected, i.e. interference between incident and reflected waves may results in a complicated wave field. By adding the velocity potentials of the incident wave φ and the reflected wave φ^r, we find the velocity potential of the resulting field.

(2-25) $$\varphi(x,t) = \varphi_{\max} \exp\left[j(\omega t - kx)\right] + \varphi^r_{\max} \exp\left[j(\omega t + kx)\right]$$

Since $p = \rho \dfrac{\partial \varphi}{\partial t}$, the pressure field in real form is:

(2-26) $$p = p_{\max} \cos(\omega t - kx) + p^r_{\max} \cos(\omega t + kx)$$

which can be written as:

(2-27) $$p = 2p^r_{\max} \cos kx \cos \omega t + (p_{\max} - p^r_{\max}) \cos(\omega t - kx)$$

The first term in the right side of Equation (2-27) corresponds to a standing wave with amplitude $2p^r_{\max}$, and the second term corresponds to a wave traveling forward with amplitude $p_{\max} - p^r_{\max}$. In the case of total refection from a plane boundary in which $p^r_{\max} = p_{\max}$, equations (2-27) becomes equation (2-28), which describes a pure standing pressure wave (Figure 2.2).

(2-28) $$p = 2p^r_{\max} \cos kx \cos \omega t$$

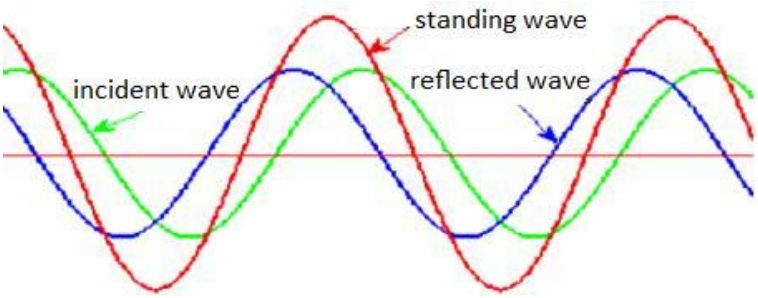

Figure 2.2. Standing wave

The amplitude of the standing wave equals twice the amplitude of the incident wave. However, the intensity of the standing wave equals zero because the energy flux in the incident wave is compensated by the backward flux in the reflected wave.

The energy distribution in the standing wave is not uniform. The pressure oscillates with maximum amplitude in planes whose coordinates satisfy the condition $x = \mathrm{n}\pi / k$, where n=0, 1, 2, 3, …. i.e. $x = \mathrm{n}\lambda / 2$ (λ is wave length of the incident wave). These coordinates correspond to antinodes of the pressure and the largest average energy density. While in planes with coordinates $x = (\mathrm{n} + \frac{1}{2})\lambda / 2$, the pressure vanishes, these planes are called nodal planes, where the average energy density equals zero.

2.3.4 Cavitation

As described previously, cavitation is the main mechanism which is responsible for most sonochemical reactions and ultrasonic surface cleaning and decontamination. It results from the large tensile stress produced by an ultrasonic wave during its rarefaction phase. To rupture a liquid and produce a cavity, the tensile stress must be above a critical value termed the cavitation threshold, p_c. In theory, p_c is determined by molecular forces only. But in practice, the presence of dissolved substances, including vapor and gases, may decrease the local strength of the liquid and form cavitation nuclei.

Cavitation intensity can be estimated by measuring the rate of hydrogen peroxide H_2O_2 formation in distilled water during sonication by a catalyzed colorimetric procedure (Mead et al., 1976). However, the generation of H_2O_2 during sonication in a fresh produce or a liquid food treatment system is complex due to the presence of food components (O'Donnel et al., 2010). There is no reliable method developed to measure cavitation activity in a food system at present (Raviyan et al., 2005). An alternative method to measure cavitation intensity is proposed by Tsukamoto et al. (2004). This method uses ultrasound amplitude as an indication of the ultrasonic cavitation.

CHAPTER 3 LITERATURE REVIEW

3.1 Literature Review

Sonic reactors and ultrasonic cleaning baths are often used in research laboratories mostly for sonochemistry studies, and they are seldom used in industry. The reasons lie mainly in the low transducer power, low energy efficiency, and lack of knowledge on reactor and cleaning tank scale up (Yasui et. al, 2007). In recent years, with the development of transducer manufacturing technique, more powerful transducers with higher energy efficiency have been developed, which makes the use of ultrasonic transducers in industrial applications possible. Researchers now become interested in the ultrasonic field distribution in ultrasonic cleaning tanks and sonic reactors in order to optimize the design and operation.

To understand the ultrasonic field distribution, one can directly measure the acoustic pressure or ultrasound generated activities, such as temperature changes and cavitation activities in a treatment chamber. Over the years, several instruments have been used to measure the acoustic field distribution in a sonic reactor, such as thermistor probes, piezo-electrical hydrophones, and aluminum foil. A thermistor measures the temperature increase at chosen points in the reactor, and hence produces a 3-D plot of energy distribution in terms of local temperature rise (Marangopoulos et al., 1995). This method is based on the theory that the increase of temperature is proportional to the local ultrasound energy density in an ultrasonic field (Martin and Law, 1980). A measurement system based on piezoelectrical hydrophones can provide the ultrasonic pressure mapping by scanning and recording pressures point by point (Jenderka and Koch, 2006). But this method is limited to low intensity ultrasound since the hydrophones are easily damaged when exposed to high ultrasound intensity. The use of aluminum foil immersed in a fluid can only provide a visual quantitative measurement of the acoustic field.

The measured values, such as sound pressure or temperature readings, by all these instruments are not the actual ones, because the instruments themselves disturb the medium

in which the measurements are made and there are multiple reflections resulting from the presence of the measure instruments (Dähnke et al., 1998).

Numerical simulation is a relatively new method used in the prediction of ultrasonic field distribution in cleaning baths and sonic reactors, which has some advantages when compared with experimental methods. Numerical simulation is less expensive and more effective in giving an idea about the sound pressure distribution in a reactor or washing tank. By using this method, the measurement work can be avoided. Secondly, numerical simulation is of great use in optimization studies. In a numerical simulation, the geometry of the sonic reactor (or the cleaning tank) and the location and parameters of the transducers can be changed easily. By comparing the different pressure distributions in different situations, the best parameters of the sonic reactor or cleaning tank and transducers can be determined (Dähnke et. al, 1999).

Numerical simulation usually uses the finite element method (FEM) to solve practical physical problems. The simulation is implemented either by using self-developed codes or by using commercial software packages.

As early as 1989, Ando and Kagawa had built a two-dimensional model to investigate the pressure distribution in a cubic ultrasonic cleaning tank (Figure 3.1), in which the radiating plate was simplified as a beam. The analysis was based on linear acoustic wave theory and cannot deal with the generation of cavitation. They took into account of the coupling effect between water and the radiator plate, and the vibration of tank walls. The coupling effect was taken into account by a coupling matrix which contained the interface information.

(3-1) $$(\frac{1}{\rho\omega^2}\hat{S}-\frac{1}{\rho c^2}\hat{M})P-Ad=\dot{V}_o,$$

(3-2) $$-A^TP+(S-\omega^2M)d=F,$$

where $\hat{S}$ is the stiffness matrix of fluid, $\hat{M}$ is the mass matrix of fluid, $\dot{V}_o$ is the driving volume displacement of fluid, P is the nodal sound pressure vector, ρ is the density of fluid, c is the velocity of sound in fluid, A is the coupling matrix, S is the stiffness matrix of the beam, d is the displacement vector of the beam, and F is the driving force vector of beam. The surface acoustic pressure at the interface of water and air was assumed to be zero. The simulation was

implemented by self-developed codes. Both the displacement of the radiator plate and tank walls and the acoustic pressure distribution in the fluid field were obtained. It was found that at the symmetric plane of the washing tank, the acoustic pressure exhibited a standing wave pattern (Figure 3.2). Since the model was two-dimensional, the result was valid only for the symmetric plane of the tank, and the vibration of the tank walls was also two-dimensional.

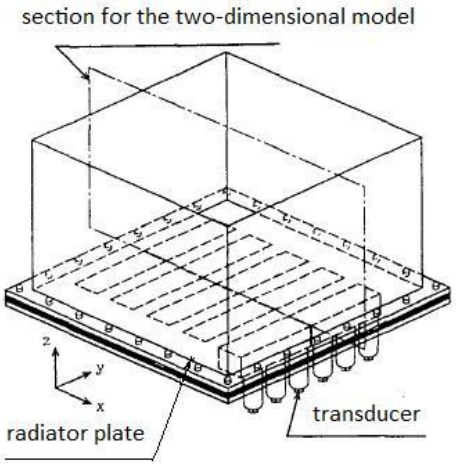

Figure 3.1. Schematic diagram of the ultrasonic cleaning tank (Ando and Kagawa, 1989)

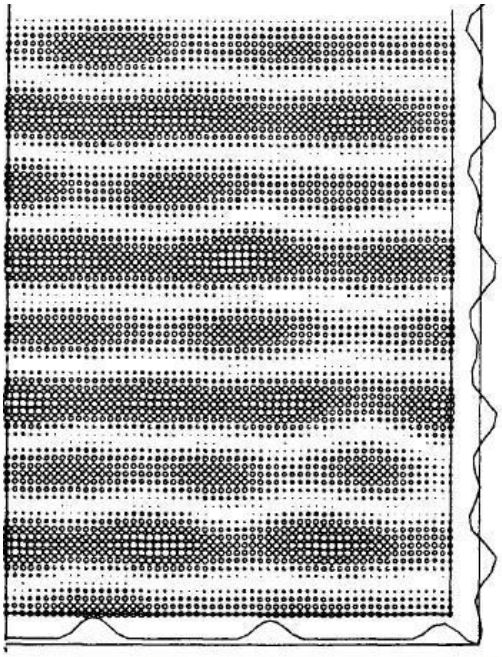

(a) Sound pressure distribution in the tank with the displacement distribution of the wall plate vibration

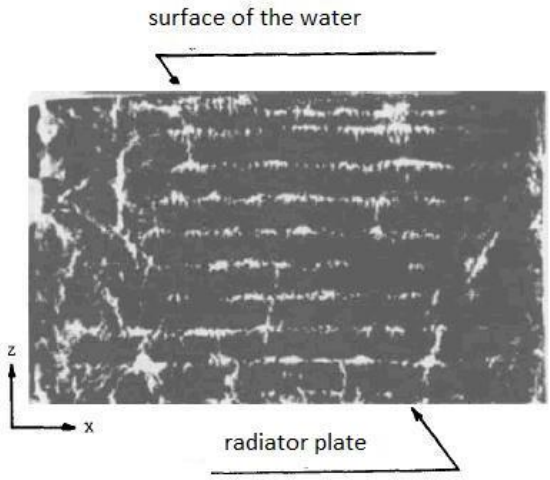

(b) The measured sound pressure distribtion in the tank

Figure 3.2. The simulation result and the measured sound pressure distribution in the tank (Ando and Kagawa, 1989)

In 1998 and 1999, Dähnke et al. conducted a series of FEM simulations of three-dimensional acoustic pressure field in cylindrical sonochemical reactors and a cubic ultrasonic cleaning tank, with or without considering the distributions of cavitation bubbles.

To calculate the pressure field in cylindrical sonic reactors (Figure 3.3) with one phase pure water, Dähnke and Keil (1998) adopted the three-dimensional, inhomogeneous Helmholtz equation (3-3) without considering the attenuation of the waves.

(3-3) $$(\Delta + k^2)\, p(r) = xx(r)$$

where Δ is the Laplace operator, k is the wave number, r is the radius of a point being interested, and $p(r)$ is the pressure amplitude. $xx(r)$ represents the input acoustic signals, which includes the acoustic primary sources and the waves which emerge from the boundaries. The acoustic pressure fields in the reactors were assumed to be a superposition of the input acoustic signal resulting from the acoustic source (transducer) into the unbounded medium and the reflecting wave field emerging from the boundaries, i.e. there was only a first-order reflection of the waves.

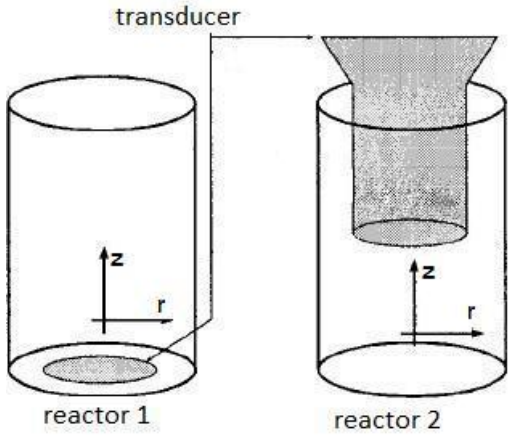

Figure 3.3. Different types of modeled sonochemical reactors (Dähnke and Keil, 1998)

The reactor walls were set to be rigid, while the surface of the fluid was set to be a "pressure release" boundary. The simulation result (Figure 3.4) at a frequency of 25 kHz gave an idea on the acoustic pressure distributions in sonochemical reactors filled with pure water. It

can be seen that the acoustic pressure decreased greatly when reaching the rigid boundary. The pressure field also showed certain standing wave pattern in reactor type 1 and 2.

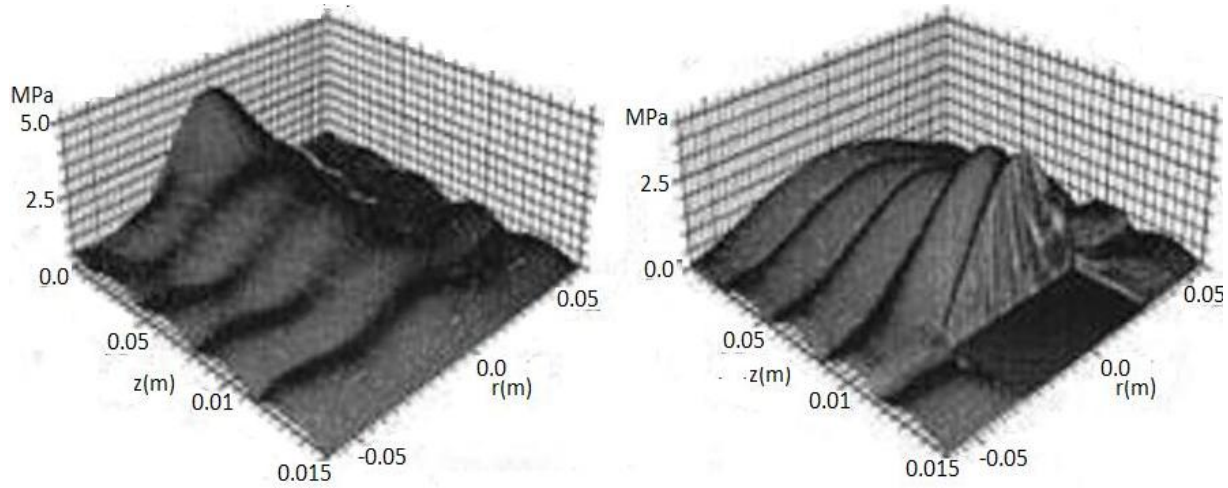

Figure 3.4. Pressure field for different types of reactors for a transducer frequency 25 kHz in pure water without cavitation bubble(Dähnke and Keil, 1998)

Dähnke and Keil (1998) also built a numerical model to calculate the pressure distributions in the same sonic reactors with an inhomogeneous density distribution of cavitation bubbles. It was assumed that no cavitation bubbles appeared below a pressure threshold of 1 MPa. The wave equation for the propagation of waves in a bubbly liquid was based on van Wijngaarden-Papanicolaou Model (3-4) and Prosperetti and Commander Theory on the distribution of bubble radii (3-5).

(3-4) $$\Delta P(r,t) - \frac{1}{c^2}\frac{\partial^2 P(r,t)}{\partial t^2} = 4\pi\rho\int_0^\infty \frac{\partial^2 R(r,R_0,t)}{\partial t^2} R_0^2 f_n(r,R_0) dR_0$$

(3-5) $$R(r,R_0,t) = R_0[1 - \frac{Q(r,t)}{\rho R_0^2}\frac{1}{\omega_0^2 - \omega^2 + 2i\alpha_0\omega}]$$

(3-6) $$\beta(r,t) = \frac{4\pi}{3}\int_0^\infty R^3(r,R_0,t) f_n(r,R_0) dR_0$$

where, $R(r,R_0,t)$ defined the instantaneous bubble radius at time *t* and positron *r*, with an equilibrium radius R_0. $f_n(r,R_0)$ was the number density of bubbles with an equilibrium radius

R_0. $Q(r,t)$ was defined by $Q(r,t) = P(r,t) - P_0$, where P_0 was the static equilibrium pressure in the liquid. ω_0 was the resonance frequency of the bubble. α_0 was a attenuation coefficient. $\beta(r,t)$ was the bubble volume fraction.

The result showed that with bubble volume fractions from 10^{-5} to 10^{-3}, for an inhomogeneous bubble density and radii obeying Gaussian distribution the acoustic field remained unchanged compared with that in pure water. While for bubble volume fraction of 10^{-2}, the structure of the field kept its original form with an amplitude decrease of approximately 20% (Figure 3.5 and 3.6). For bubble volume fraction of 2×10^{-1} which is rare in practice, the acoustic field kept its original structure in the vicinity of the transducer, and then decreased quickly. While at places far from the wave source, the wave showed an undamped propagation.

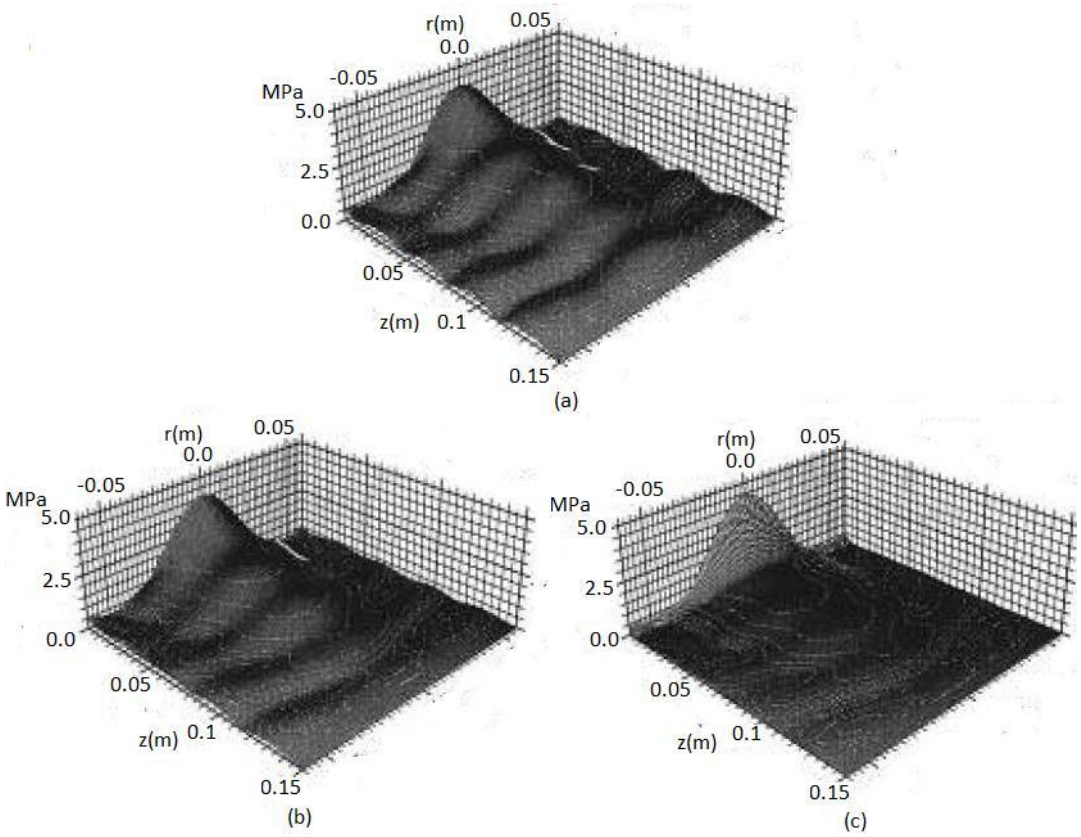

Figure 3.5. Pressure field of reactor type 1 for a transducer frequency of 25 kHz and an assumed cavitation threshold of 10^6 Pa, and different inhomogeneous gas bubble void fractions: (a) $\beta_1 = 10^{-3}$, (b) $\beta_2 = 10^{-2}$, and (c) $\beta_1 = 2\times10^{-1}$ (Dähnke and Keil, 1998)

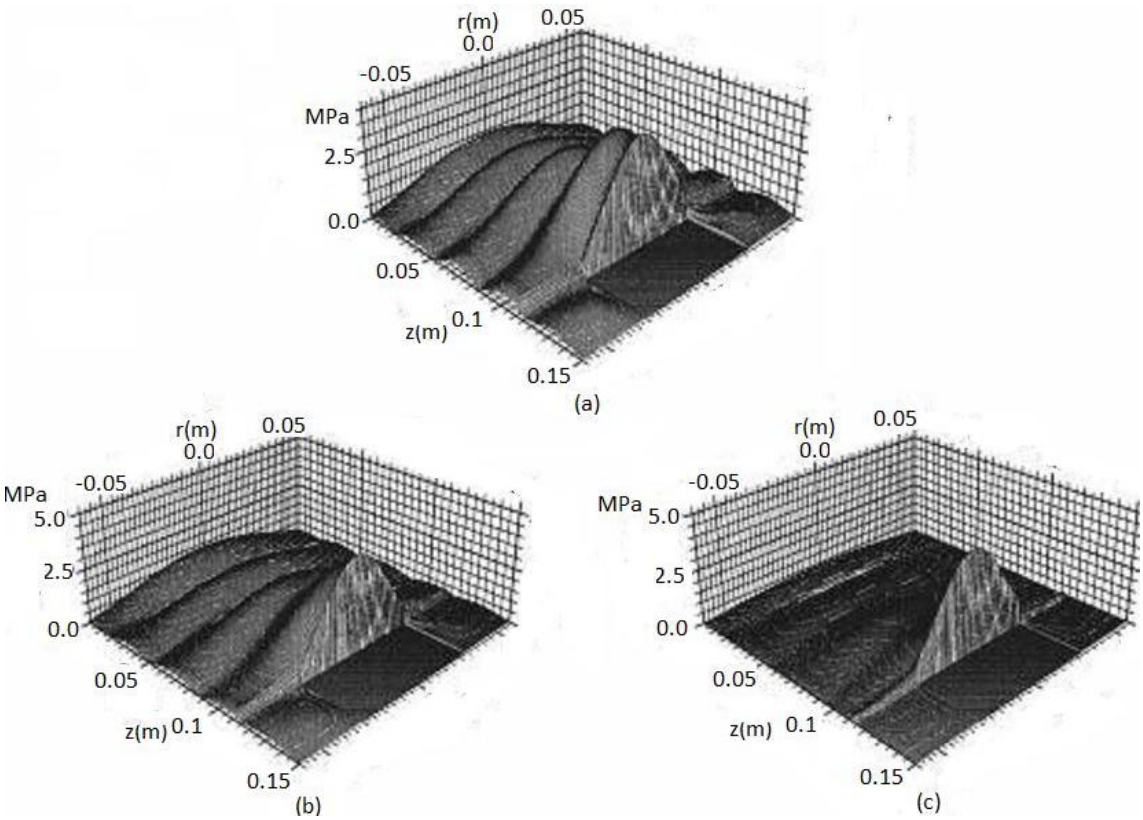

Figure 3.6. Pressure field of reactor type 3 for a transducer frequency of 25 kHz and an assumed cavitation threshold of 10^6 Pa, and different inhomogeneous gas bubble void fractions: (a) $\beta_1 = 10^{-3}$, (b) $\beta_2 = 10^{-2}$, and (c) $\beta_1 = 2 \times 10^{-1}$ (Dähnke and Keil, 1998)

All the calculations were carried out for transducer frequencies of 25 and 50 kHz, by self-developed codes. The resulting pressure fields were in steady-state conditions, which mean the parameters of the pressure fields remain constant in time- and space- domains. There was no experimental pressure field presented for comparison. In their work of modeling a three-dimensional acoustic pressure field in a cubic sonochemical reactor (Figure 3.7) with inhomogeneous density distribution of cavitation bubbles, Dähnke et al. (1999) adopted an inhomogeneous wave equation modified from the homogeneous wave equation, by multiplying one specific harmonic solution $p(x,t) = e^{i(kx-\omega t)}$ by an exponential damping term $e^{-\alpha_0 x}$, then developing the result into three dimensions.

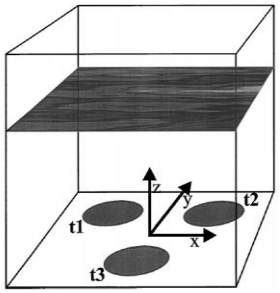

Figure 3.7. Modeled sonochemical reactor (t1, t2 and t3 are the locations where three transducers are installed)(Dähnke et al., 1999)

The initial condition was described with zero pressure amplitude at the time zero and a harmonic change of a pressure distribution at the surfaces of the three transducers. At the four boundary walls of the tank, the incident wave was assumed a total reflection with a phase shift. The water-air interface was assumed a pressure-release face.

By finite difference method, the whole pressure distribution field was finally calculated for 12 periods. The calculated pressure field distribution was compared with the measured pressure field distribution (Figure 3.8). The result shows that along the center axis of each transducer, the acoustic pressure amplitude obeyed a standing wave pattern. In the whole washing tank, the acoustic pressure field was not uniform, but better than that in the cylindrical reactors.

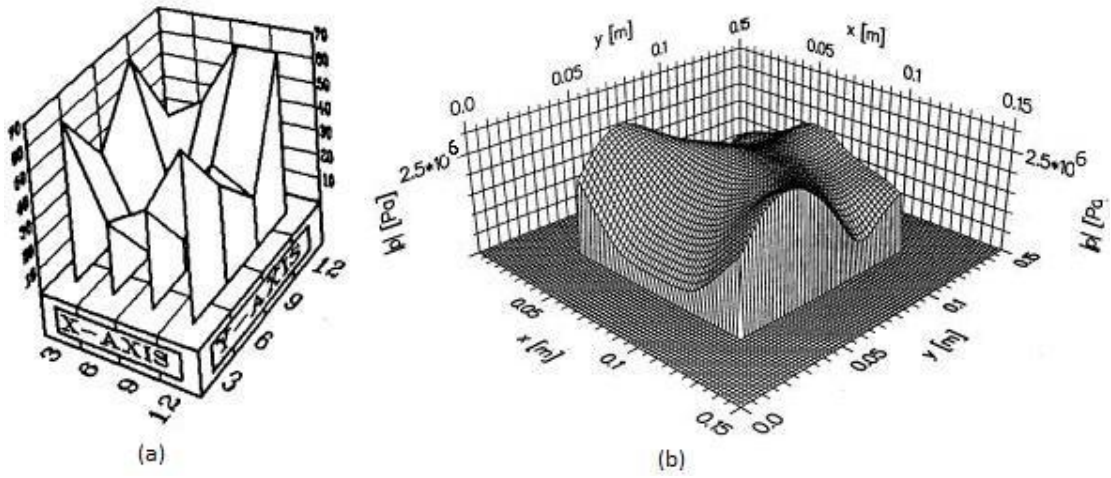

Figure 3.8. Comparison of the pressure field distribution in the plane with a height of 0.04m above the xy-plane: (a) measured pressure amplitude, (b) simulated pressure amplitude (Dähnke et al., 1999)

Sáez et al. (2005) carried out a numerical simulation of the ultrasonic pressure distribution in a cylindrical sonoreactor (Figure 3.9) at frequency 20 kHz. The wave equation they adopted was the homogeneous space-dependent Helmholz equation (3-7)

(3-7) $$(\Delta + k^2)p(r) = 0 .$$

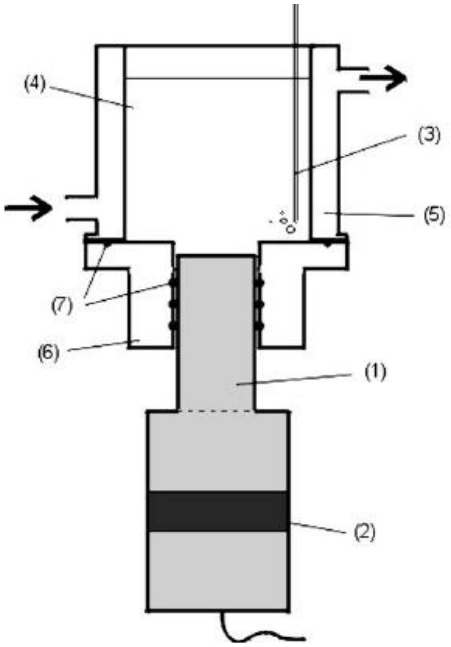

Figure 3.9. Diagram of the experimental set-up: (1) ultrasonic probe, (2) transducer, (3) gas passing, (4) water, (5) cooling jacket, (6) Teflon adapter, and (7) O-ring joints (Sáez et al., 2005)

The boundary conditions of the model were set as: at the water-air interface, $p = 0$; at the cylinder wall, $\delta p / \delta n = 0$ (rigid wall); and at the transducer probe surface, $p = p_0$. The simulation was implemented by a commercial finite element software package FEMLAB 3.0, with the acoustic frequency $f = 20\text{kHz}$. The simulation result (Figure 3.10) was compared with the effect of the ultrasound on the erosion of an aluminum foil (Figure 3.11). Both results showed that the ultrasound distribution in the reactor was to certain extend like that in the cylindrical reactor Dähnke and Keil (1998) simulated, except for being even nonuniform.

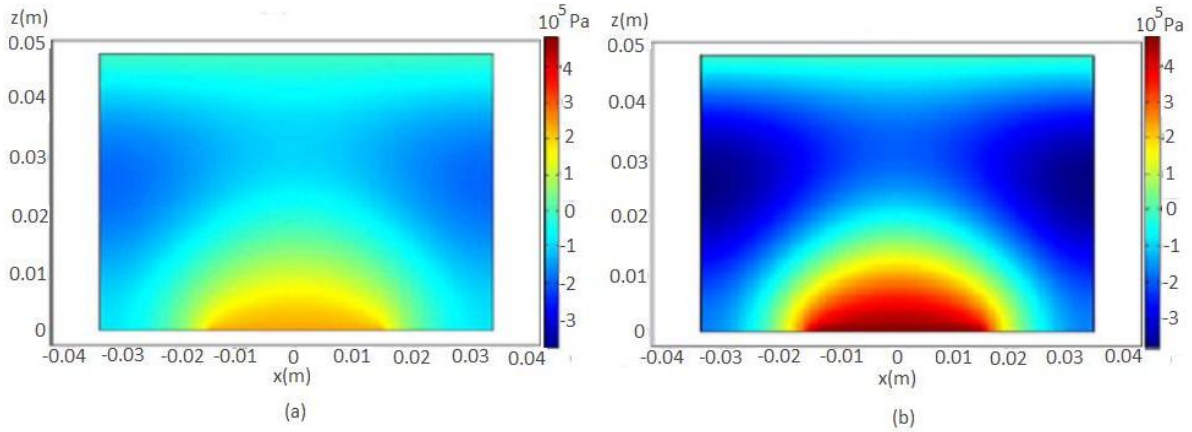

Figure 3.10. Acoustic pressure field distribution for a circular plane piston transducer: radius=15mm, working at 20 kHz; (a) global ultrasonic intensity 1.84 W cm^{-2} and (b) 7.64 W cm^{-2} (Sáez et al., 2005)

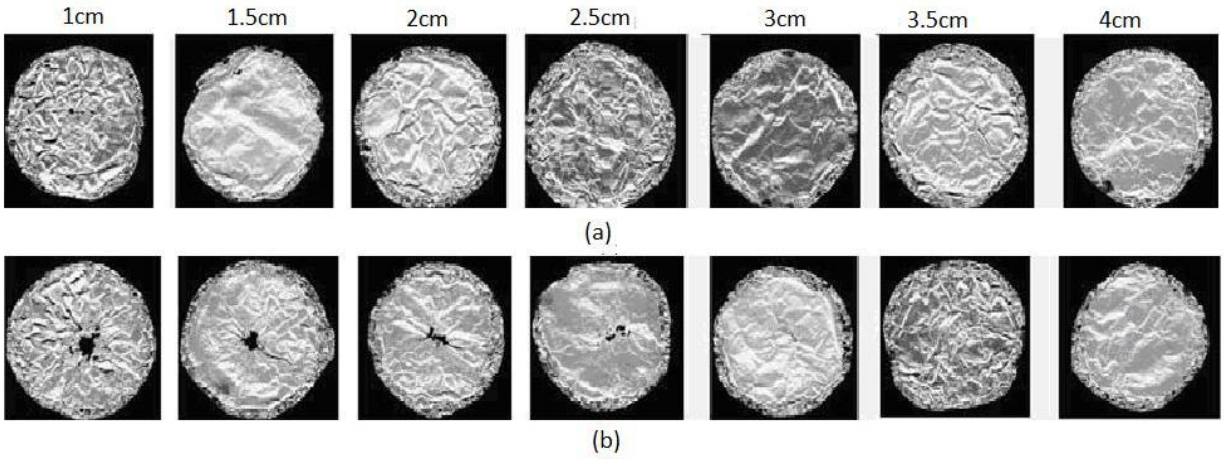

Figure 3.11. Effect of the ultrasound intensity on the erosion of an aluminum foil placed parallel to the emitter surface at different global ultrasonic intensities: (a)1.84 W cm^{-2} , (b)7.64 W cm^{-2}) and foil-emitter surface distances (1- 4 cm) (Sáez et al., 2005)

Bretz et al. (2005) conducted a numerical simulation of ultrasonic waves in a standing cylindrical cleaning tube by a two-step procedure combining a harmonic and transient computation. They used a wave equation set based on the sound wave equation propagating in a bubbly liquid (3-8) and the Gilmore equation (3-9) describing the radial dynamics of the cavitation bubbles in dependence of the pressure of the mixture.

(3-8) $$\frac{1}{c_f^2}\frac{\partial^2 p}{\partial t^2} - \nabla^2 p = \frac{4}{3}\pi\rho_f f_n[6R\dot{R}^2 + 3R^2\ddot{R}]$$

(3-9) $$R(1-\frac{\dot{R}}{C})\ddot{R}+\frac{3}{2}(1-\frac{\dot{R}}{3C})\dot{R}^2=(1+\frac{\dot{R}}{C})H+\frac{R}{C}(1-\frac{\dot{R}}{C})R\frac{dH}{dR}$$

The bubble number density f_n was assumed a constant. The bubble radius R was variable dependent on the acoustic pressure. C was the sound speed in the liquid at the bubble wall, and H was the enthalpy difference between the liquid at the bubble wall and far away from the bubble and is depending on the pressure determined above.

In implementing the numerical simulation, the steady state was computed first, in which cavitation was neglected. Then the result was used as initial input data for the transient simulation using the cavitation model. A self-developed finite element code CFS++ was used to solve the wave propagation in time domain over five periods. This simulation was coupled directly with the computation of the mechanical vibration in the solid boundary. The Gilmore equation was solved by an embedded Runge-Kutta-Method of 5th Order.

The computed acoustic pressure field was shown in Figure 3.12, compared with the measured pressure amplitude and an eroded aluminum foil which had been put into the pressure field for 4 minutes. Compared with the work of Dähnke and Keil (1998) and Sáez et al. (2005), it was obvious that the change of boundary conditions (a rigid one to a soft one) would result in great change of the acoustic pressure field structure in a cylindrical reactor.

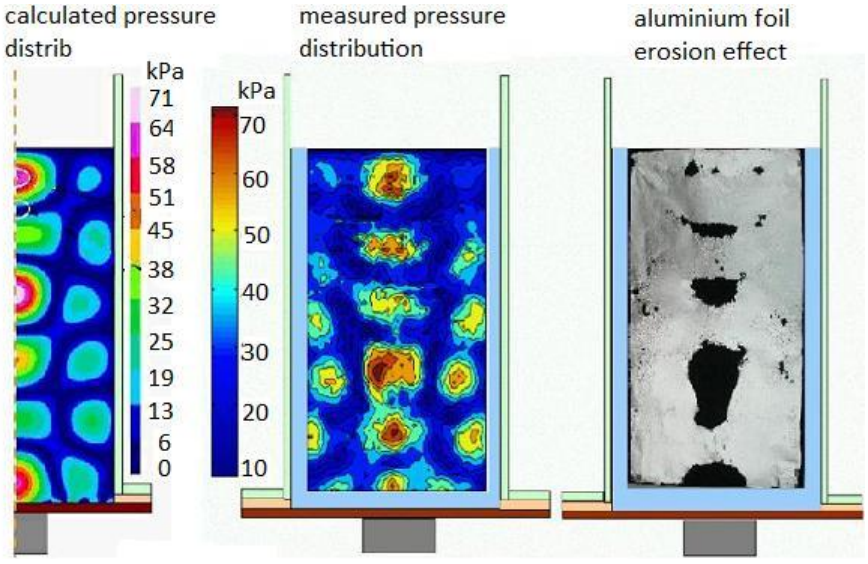

Figure 3.12. Comparison of the simulation result and the measured result (Bretz et al., 2005)

Klíma et al. (2007) performed a geometry optimization of a 20 kHz sonoreacator on the basis of numerical simulation. The equation they used was the linear Helmholtz equation. As for the boundary conditions, they set $p = 0$ at the water-air interface and walls of the glass reactor, $p = p_0$ at the horn tip, and $\delta p / \delta n = 0$ at the side-walls of the horn. The boundary conditions mean that the entire ultrasonic energy enters the reactor through the horn tip-face, whereas the side-walls of the horn were rigid; the glass walls of the reactor were ignored, i.e. the pressure vanished at the glass wall. To solve Helmholtz equation, a commercial finite element software package FEMLAB 3.1 was used. There was a comparison between the photograph of cavitating bubbles and simulated intensity distribution in the optimized reactor (Figure 3.13). The simulation result showed that small changes in the horn position and/or liquid level varied the ultrasound distribution to a great extent.

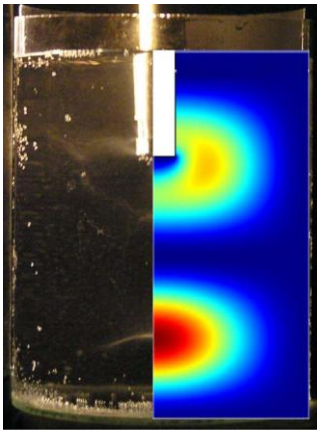

Figure 3.13. Photograph of cavitating bubbles in the optimized cell (water, 20kHz, P=10 W) (Klíma et al., 2007)

Yasui et al. (2007) carried out a FEM calculation of an acoustic field in a rectangular sonic reactor to investigate the influence of boundary conditions and attenuation coefficient on the acoustic field distribution in the reactor. The bottom of the reactor was a vibrating plate which vibrated at frequency of 100 kHz. In this simulation, they neglected the spatial distribution of bubble number density in bubbly water and assumed that the attenuation coefficient of ultrasound in bubbly water was spatially uniform. They also neglected the effect of cavitation

bubbles on the ultrasound velocity, which meant that linear wave equations were used with an attenuation coefficient.

The attenuation effect was took into account by defining a complex sound velocity

(3-10) $\tilde{c} = \omega / \tilde{k}$,

where ω is the angular frequency of ultrasound,

(3-11) $\tilde{k} = k - i\alpha_0$,

where $k = \omega / c$ is the wave number, c is the wave velocity in the medium, and α_0 is an uniform attenuation coefficient of the ultrasound in the medium. The coupling effect of the acoustic field and the vibration of the reactor's walls was taken into account by assembling the FEM wave equation and the FEM solid vibration equation. The implement of the simulation was carried out by the commercial FEM software, PAREC-vibroacoustics. The result was for a steady wave state. As for the boundary conditions, at the liquid surface and the outer surface of the reactor's walls, the acoustic pressure was set to be zero. At the vibrating plate where ultrasound generated, an oscillating displacement of Gaussian distribution was applied.

It was found that a standing wave pattern was formed in the rectangular reactor when the attenuation coefficient is in the range of 0.5-5 m^{-1}, and that the thin glass or stainless steel wall was nearly a free boundary, while the thick glass or stainless steel wall was nearly a rigid boundary. It was also found that when the attenuation coefficient was less than about 0.05 m^{-1}, the acoustic field in the liquid is very complex due to the acoustic emission from the vibrating wall.

Louisnard et al. (2009) made a series of simulations of the steady state acoustic pressure distribution in a sonoreactor (Figure 3.14) accounting for vibrations of the boundaries and the attenuation effect of bubbles. The linear wave equation was used. By using the complex wave-number $\tilde{k}$ in equation (3-11), the attenuation of the wave was taken into account. In the simulation, α in equation (3-11) was set to be a variable, but spatially uniform.

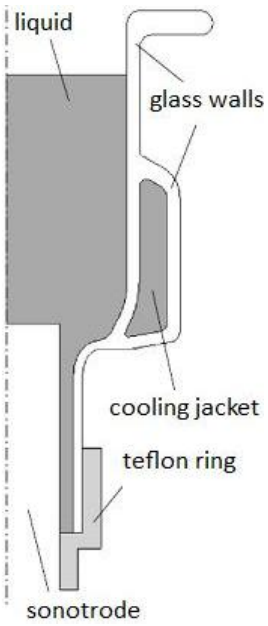

Figure 3.14. Experiment setup (Louisnard et al., 2009)

The boundary conditions were as follows:

For air-water interface, p=0. On the radiating surface of the transducer,

(3-12) $$\nabla P \bullet n = \rho_1 \omega^2 U ,$$

where P is the complex notation of the liquid pressure, n is the normal pointing outward the liquid, U is the complex amplitude of the transducer displacement. For liquid-solid interface,

(3-13) $$\nabla P \bullet n = \rho_1 \omega^2 U_s \bullet n ,$$

where U_s is the displacement of the solid. The problem defined above was solved by the commercial software COMSOL.

Louisnard et al. found that in the case of attenuation absent, there were several resonant frequencies for the whole mechanical system formed by the liquid and the solid walls at which the mean acoustic pressures in the reactor were extremely high, and the deformation of the reactor was big too. They also noticed that exciting the sonoreactor near a resonant frequency might help to prevent the pressure antinode appearing near the sonotrode.

They investigated the influence of attenuation coefficient on the acoustic pressure distribution, and found that attenuation influenced both the amplitude of the acoustic pressure and the structure of the acoustic field, such as the antinode location.

3.2 Objectives

The overall objective of this study was to investigate the ultrasonic pressure distribution in a ultrasonic treatment chamber, which can be used to direct the design modification and optimization, as well as the operation of an ultrasound treatment for food processing and preservation purposes.

Computational models using FEM and a commercial multi-physics software were employed in the simulation studies where two typical ultrasonic treatment set-ups were analyzed; one was a sonoreactor and the other was an ultrasonic washing tank.

The specific objectives were:

1. To investigate the acoustic pressure distribution and intensity distribution in the sonoreactor and the ultrasonic washing tank with multi-physics software Abaqus by including the coupling effect between the solid wall and the ultrasound medium;

2. To find the optimal position of the ultrasonic probe along the axis of the sonoreactor so that the ultrasound intensity distribution in the reactor was as uniform as possible to maximize the microbial inactivation efficacy;

3. To study the effect of ultrasound emitting element location on the distribution of acoustic pressure in the washing tank with Abaqus;

4. To verify the simulation results by microbial inactivation tests for the sonoreactor and by the aluminum foil method for the washing tank.

CHAPTER 4 EXPERIMENTAL METHODS

In this study parametric simulations were conducted using Abaqus as a design and analysis tool, and Matlab as a data post-process tool. The investigation was focused on parameter optimization to obtain a uniform acoustic pressure distribution.

To implement the simulation of acoustic pressure distribution in an ultrasonic reactor or a washing tank, both self-developed codes and commercial software packages can be used. Generally, if the use of available commercial software can satisfy all the requirements in the simulation, there is hardly a need to use self-developed codes.

4.1. Comparison of Commercial Software Packages

Several commercial software packages were compared with regard to their capacity in solving sound wave propagation problems. It was found that in dealing with ultrasound propagation problems, Abaqus can meet most of the requirements of this study, such as pressure amplitude variation, multiple frequencies mixture, temperature changes, etc. The functions of 5 selected software packages are listed in Table 4.1.

Table 4.1. Function of selected commercial software packages.

Requirement	Abacus[a]	COMSOL[b]	PAFEC VibroAcoustics[c]	Ansys/ Fluent[d]	FEM Self-developed code
Change frequency					
-single	Yes	Yes	Yes	Yes	Yes
-multiple	Yes	No	No	No	Yes
Change T	Yes	No[e]	No[e]	Info not	No[e]
Change P	Yes	No[e]	No[e]	available	No[e]

Table 4.1. (cont.)

Fluid Property -viscosity -surface tension -vapor pressure -dissolved gas	 Yes Yes No No	Info not available	 No No No No	Info not available	 Yes Yes
Flow velocity	Yes (bulk uniform velocity)	No	No	Info not available	Yes
Cavitation	Yes. By setting up a P value.	Use attenuation factor	Use attenuation coefficient	Info not available	Damping coefficient
Consider cavitation by introducing a bubble phase	Cannot handle	Need to coupled with CFD	Cannot handlee	Helmholtz equation + Bubble dynamics equation	Helmholtz equation + Bubble dynamics equation

a. Based on FEM. Can only use an acoustic element in the analysis fluid domain.
http://www.simulia.com/index.html
b. Based on FEM. Can do the fluid only, or coupled with reactor wall vibration.
http://www.comsol.com/
c. Based on FEM. Solve wave equations coupled with reactor wall vibration equations.
http://www.vibroacoustics.co.uk/
d. http://www.ansys.com/products/fluid-dynamics/fluent/.
e. Some of the simulation tools may accommodate self-developed code to expand its capacity. In that case, more parameters, such as temperature and viscosity, might be treated as variables.

4.2. Model Setup

4.2.1 Experimental Setup

Two sets of experiments were conducted in this study for simulation and validation purposes. The first was an ultrasound probe system to test the microbial inactivation efficacy of ultrasound in combination with other decontamination methods (Figure 4.1). The main equipment is a cylindrical sonoreactor (Figure 4.2). The purpose of the simulation was to find

the optimized position of the probe along the axis of the sonoreactor filled with 40 ml water so that the ultrasound intensity distribution in the reactor was as uniform as possible to maximize the microbial inactivation efficacy.

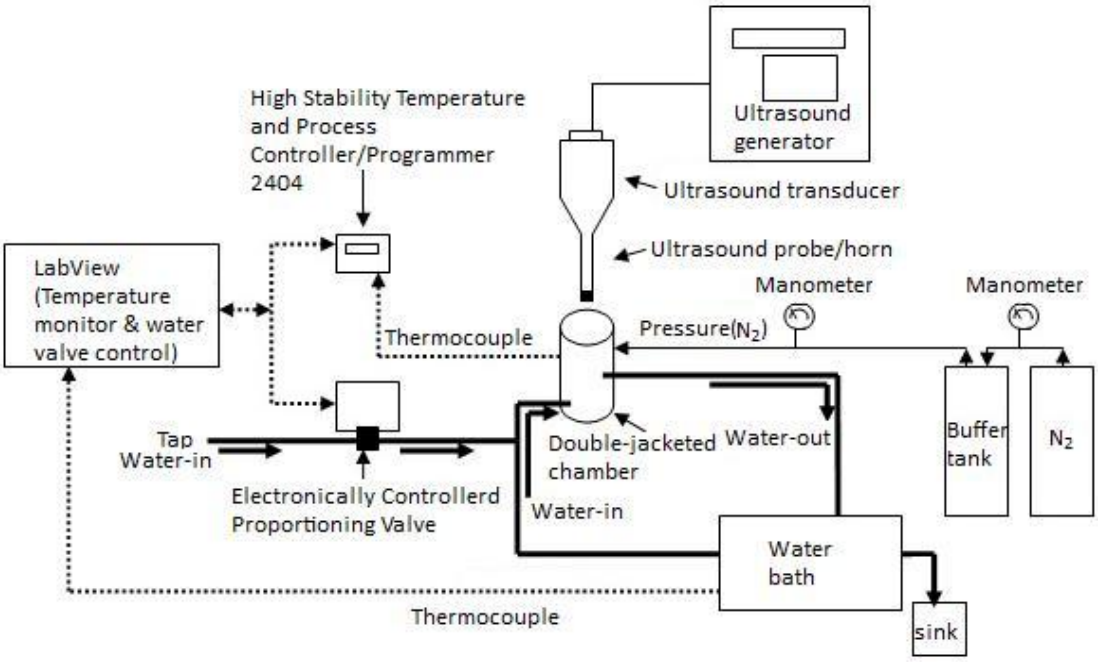

Figure 4.1. The Sonoreactor system for inactivation tests

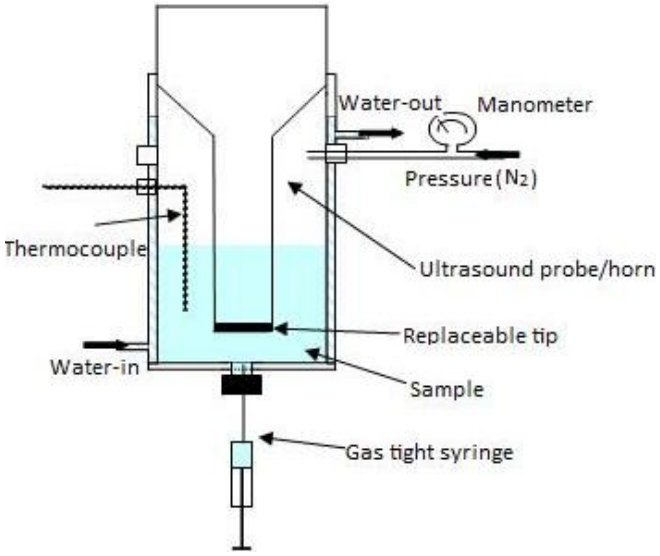

Figure 4.2. The sonoreactor for inactivation tests

The second setup was a novel ultrasonic washing tank built for surface decontamination purposes (Figure 4.3). Three pairs of ultrasound transducer boxes were installed in the washing tank to form a channel. For each pair, two parallel transducer boxes with a distance of 30 cm (Figure 4.4) were fixed to a frame attached to the tank and immersed in water. For each transducer box, there were twelve ultrasound transducers glued onto the inner face of the metal box. The two boxes were set face to face so that the ultrasound propagated towards each other. It is believed that the ultrasound field between the two boxes is relatively uniform and hence has an improved decontamination effect. The purpose of this simulation was to understand the ultrasound field distribution and validate its efficacy of reduction of pathogen population.

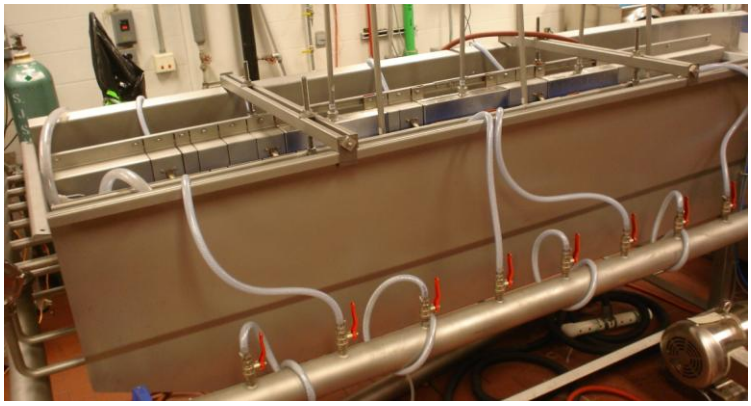

Figure 4.3. The washing tank with an ultrasound channel embedded

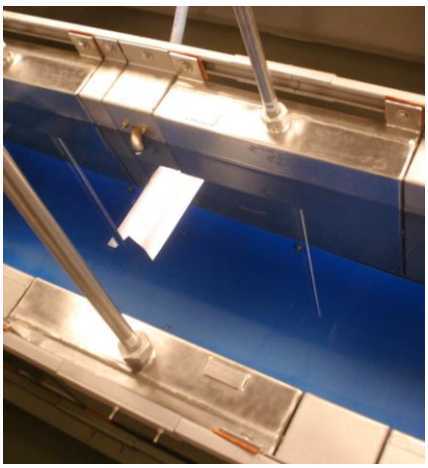

Figure 4.4. A pair of transducer boxes

4.2.2 Simplifications

For the sonoreactor, the ultrasonic horn was connected to the upper side wall of the reactor by a screw joint at a location that was a half wavelength (λ/2) node and immersed in water to a pre-determined depth. This installation ensured that there was no vibration delivered to the sonoreactor wall. Since the intention of this simulation was focus on the ultrasound pressure field in the reactor, to simplify the model, the horn or delivery system as shown in Figure 1.3 was not considered in this simulation. Besides, the tubes to let in (or out) water, thermocouple, monometer, and syringe were neglected too. The model includes only the cylindrical reactor and water.

The washing tank is consisted of the tank, the six transducer boxes, the frame to support the transducer boxes, and the water inlets and outlets. In practical, the vibration of the transducers might be able to cause a system resonance vibration which can influence the acoustic pressure distribution in the washing tank. However, it is impracticable to include all parts of the system in the simulation. To save computation time and accommodate simulation with a desk-top station, only the space between two parallel stainless steel boxes (with one side open for simplification of jointing, without transducers) and a block of water with a cubic geometry was chosen as the numerical analysis domain.

4.2.3 Model Setup

The sonoreactor is made of stainless steel, open on the upper side and closed at the bottom. The dimensions of the reactor and water are shown in Figure 4.5.

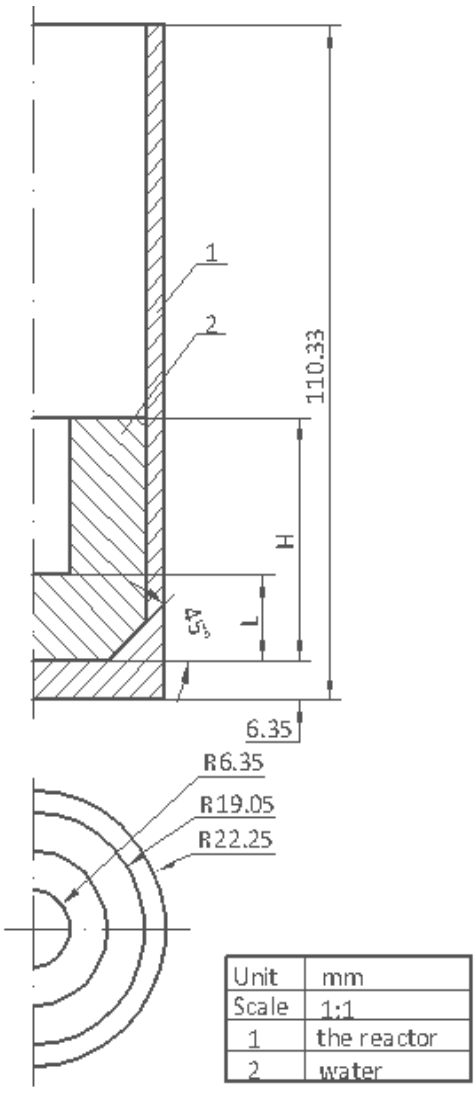

Figure 4.5. Model of the sonoreactor

Since the purpose of this simulation was to find the optimized position of the probe along the axis of the sonoreactor, the distance L between the inner bottom of the reactor and the tip surface of the probe was changed from 2 mm to 30 mm, while the volume of water was kept unchanged at 40 ml. The values of L and the corresponding height of water H are listed in Table A.1.

In the model of the washing tank (Figure 4.6), the transducer box was made of stainless steel plate, with a thickness of 2 mm. In this simulation, the symmetric dimension was utilized--only half of one transducer box and one-fourth of the water were included.

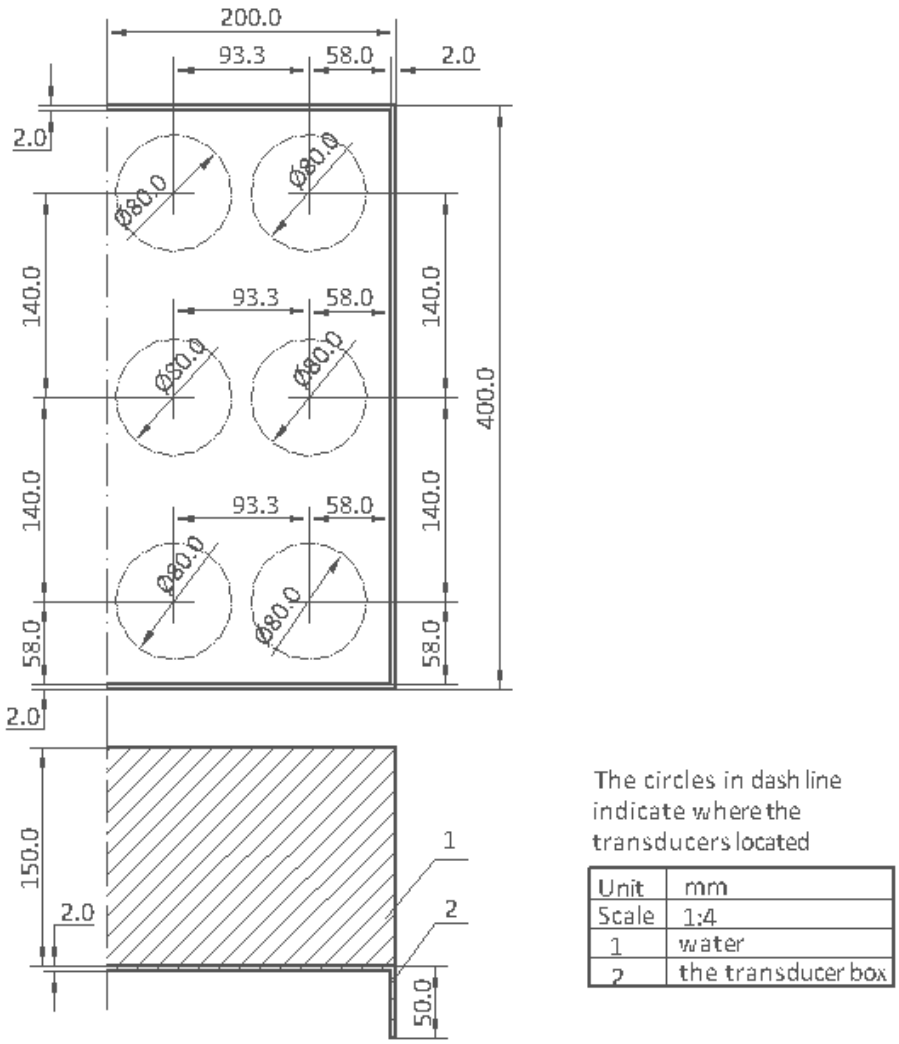

Figure 4.6. The model of the washing tank

4.3. Mathematical Model

4.3.1 Wave Equations

To simulate the ultrasound pressure amplitude distribution in sonoreactors by finite element method, the wave propagation phenomena such as divergence, scattering, energy dissipation, wave reflection and transmission, especially the nonlinear ultrasound phenomena such as cavitation, acoustic streaming, and acoustic radiation pressure should be considered.

In reality, while the effect of wave divergence, scattering and energy dissipation can be represented by a wave attenuation coefficient, there is no proper formulation that can include the complexity of cavitation, streaming, and acoustic radiation pressure, including the formation of bubbles, the implosive effect of cavitation on the acoustic field, and the energy transformation from wave energy to instantaneous high pressure and high temperature during bubble collapse.

However, though practical ultrasound propagation is nonlinear and complex, it has been reported in the literature that a linear wave propagation simulation with a proper attenuation coefficient may give a good approximation of the distribution of ultrasound pressure field in a sonoreactor, with relatively simple theory and less expenses in calculation. In this simulation, the wave equation provided by Abaqus for small motions of a compressible, inviscid, adiabatic, linear behavioral fluid in 3-dimension is as follows:

(4-1) $$\frac{\partial p}{\partial X} + \gamma_{(x,\theta_i)}\dot{u} + \rho_{f(X,\theta_i)}\ddot{u} = 0$$

where, p is the excess pressure in the fluid (the pressure in excess of static pressure); u is the displacement of fluid particle from equilibrium position; $\dot{u}$ is the fluid particle velocity; $\ddot{u}$ is the fluid particle acceleration; X is the spatial position of the fluid particle; γ is the "volumetric drag" which causes the wave to have a particle-velocity-dependent dissipation, i.e. the effect of γ is the like the attenuation coefficient, and ρ_f is the density of the fluid. Both γ and ρ_f could be functions of spatial position and other independent filed variables such as temperature, while in this simulation, γ and ρ_f were set to be constants.

The constitutive behavior of the fluid is given by

(4-2) $$p = -K_{f(X,\theta_i)}\frac{\partial}{\partial X}\bullet u$$

where K_f is the bulk modulus of the fluid, which could be a function of spatial position and other independent field variables. In this simulation, K_f is set to be a constant.

4.3.2 Analysis Procedure

Abaqus provides two classes of analysis procedures, the linear perturbation analysis procedure and general analysis procedure. A general analysis procedure refers to those where the responses can be either linear or nonlinear during the analysis, while a linear perturbation procedure is for analyses in which only linear responses are generated.

In general, a simulation with acoustic elements is treated as small-displacement linear perturbation analysis, in which the strain in the acoustic elements is volumetric and small. In this situation, a steady-state dynamic analysis is used to get the steady-state amplitude and phase of the response of a system due to harmonic excitation at a given frequency.

For a high frequency steady-state acoustic-structural response using nodal degrees of freedom, the direct-solution steady-state dynamic analysis procedure is to be preferred over the mode-based procedure since the volumetric drag is significant. Furthermore, in the direct-solution steady-state dynamic harmonic response procedure, the gradient of γ / ρ_f needs not be small, and the acoustic-structural coupling and damping are not restricted, as in other types of steady-state analysis procedures (Abaqus, 2007).

A direct-solution steady-state analysis procedure calculates the harmonic response of the acoustic-structural system directly in terms of the physical degrees of freedom of the model, by using the mass, damping, and stiffness matrices of the system. The formulation forms a large linear system of equations defining the coupled structural-acoustic mechanics at a single frequency. The result calculated by a direct-solution steady-state analysis is more accurate than that calculated by a mode-based or a subspace-based steady-state dynamics analysis procedure. In this simulation, a steady-state response analysis procedure was used.

In a steady-state response analysis procedure, all model degrees of freedom and loads were assumed to be varying harmonically at an angular frequency ω. Equation (4-1) and (4-2) can be written as:

(4-3) $$\frac{\partial \tilde{p}}{\partial X} - \omega^2(\rho + \frac{\gamma}{i\omega})\tilde{u} = 0$$, and

(4-4) $$\tilde{p} = -K_{f(X,\theta_i)} \frac{\partial}{\partial X} \bullet \tilde{u} .$$

The combining of equations (4-3) and (4-4) yields:

(4-5) $$\omega^2 \frac{1}{K_f} \tilde{p} - \frac{\partial}{\partial X} \bullet (\frac{1}{\tilde{\rho}} \frac{\partial \tilde{p}}{\partial X}) = 0 \text{ and}$$

(4-6) $$\tilde{\rho} \equiv \rho_f + \frac{\gamma}{i\omega}$$

where, $\tilde{p}$ is the constant complex amplitude of p, and $\tilde{\rho}$ is the complex density of the fluid. Equations (4-5) and (4-6) are the wave equation used in Abaqus for a steady-state wave analysis.

4.3.3 Volumetric Drag

During acoustic wave propagation, fluids exhibit momentum losses due to the energy transformation from wave to heat. This energy transformation is caused by shear viscosity and bulk viscosity. The shear viscosity coefficient μ characterizes viscous losses accompanying shear deformation rate, while the bulk viscosity coefficient η is relative to the volume compression rate (Shutilov, 1988). For a propagating plane wave with nominal particle velocity $\dot{U}$, the energy loss rate can be represented as

(4-7) $$\dot{E} = \gamma [\dot{u}]^2$$

where γ is a combined coefficient representing the attenuation effect of both shear viscosity and bulk viscosity, and is called volumetric drag coefficient.

In fluid mechanics the shear viscosity term is much more important than the bulk viscosity term; however, acoustics is the study of volumetrically straining flows, so both constants are important in acoustic problems (Shutilov, 1988). To derive the expression of volumetric drag coefficient γ, we can start form the linearized Navier-Stokes equation for adiabatic perturbations about a base state (Abaqus, 2007)

(4-8) $$\frac{\partial}{\partial X} \bullet \frac{\partial p}{\partial X} = \frac{\rho_f}{K_f} \ddot{p} - \frac{\eta + \frac{4}{3}\mu}{K_f} \frac{\partial}{\partial X} \bullet \frac{\partial \dot{p}}{\partial X} .$$

In steady state this equation can be written as:

(4-9) $$\Delta\tilde{p}(1+i\omega\frac{\eta+\frac{4}{3}\mu}{K_f})+\omega^2\frac{\rho_f}{K_f}\tilde{p}=0\,.$$

By analogizing equations (4-3) and (4-6), the volumetric drag coefficient is determined as:

(4-10) $$\gamma=\left[\frac{\left(\frac{\omega}{K_f}\right)^2(\eta+\frac{4}{3}\mu)}{1+\left(\frac{\omega}{K_f}\right)^2(\eta+\frac{4}{3}\mu)^2}\right]\rho_f K_f\ .$$

If the combined viscosity effects are small,

(4-11) $$\gamma=\frac{\omega^2\rho_f}{K_f}(\eta+\frac{4}{3}\mu)\,.$$

The shear viscosity of water at 4 °C is $\mu=1.6\times10^{-3}P_a\cdot S$, and the bulk viscosity of water at the same temperature is $\eta=6.2\times10^{-3}P_a\cdot S$ (Xu et al., 2003). At an angular frequency of 125,664 rad/s (20 kHz), the volumetric drag coefficient of water is about 59.988 $P_a\cdot S$ according to equation (4-11).

4.4. Material Properties

Both the cylindrical sonoreactor and the transducer box were made of stainless steel. The acoustic medium was water. The operation temperature was 4 °C. The mechanical and/or acoustic properties (at temperature 4 °C) of both materials are listed in Table 4.2, in which the acoustic wave speed is calculated according to equation (4-11).

(4-11) $$c=\sqrt{K/\rho}$$

where K is the bulk modulus of the medium in which the acoustic wave propagates, and ρ is the density of the medium.

Table 4.2. Material Properties

Material	Density (kg / m^3)	Young's Modulus (GPa)	Bulk Modulus (GPa)	Poisson's Ratio	Acoustic Wave Speed (m/s)
Stainless Steel	8000	200	160.0	0.3	5060
Water	1000	----	2.2	---	1480

4.5. Mesh Generation

The analysis domain was meshed using Abaqus/CAE, which is a preprocess software package of Abaqus. The water was meshed with acoustic element, while the reactor and the transducer boxes were meshed with stress/displacement element. These two types of elements were adopted in order to involve the dynamic interactions between the liquid acoustic medium and the solid structure.

Several sets of mesh were tested to get good quality of the tetrahedrons. In order to minimize the effect of mesh quality and size on the results, different meshes were used with increasing mesh density until the mesh change had little effect on the simulation results. The criteria which were used to control the element quality are listed in Table 4.3.

Table 4.3. Element Quality Control Criteria

Selection Criterion	Hexahedra	Tetrahedra
Shape Factor (SF)	N/A	0.01
Smaller face corner angle	15	110
Larger face corner angle	160	160
Aspect ratio	5	5

For tetrahedral elements the shape factor was defined as:

(4-12) $$SF = \frac{EV}{OEV}$$

where *EV* is the element volume, *OEV* is the optimal element volume. The optimal element volume is the volume of an equilateral tetrahedron with the same circumradius as the element being evaluated. The aspect ratio is the ratio between the longest and shortest edge of an element.

In the model of cylindrical sonoreactor, there were totally about 64,600-76,500 acoustic elements for water, and 48,000 stress/displacement elements for the reactor (Figure 4.7). The size of the edge of the stress/displacement elements was about 2 mm. For acoustic element, the edge size was from 1 mm to 2 mm, which was smaller than the stress/displacement element size. Smaller acoustic elements were used near the ultrasound probe where acoustic pressure gradient is supposed to be higher. The geometric order for both acoustic element and stress/displacement element was linear.

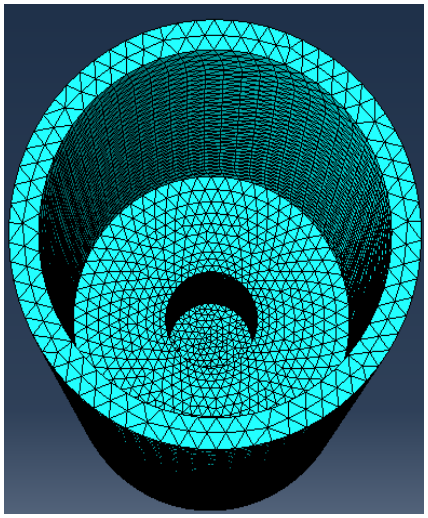

Figure 4.7. Mesh of the sonoreactor model

In the model of the washing tank, there were totally about 768,050 acoustic elements for water with an average element size of 2.5 mm, and 83,150 stress/displacement elements for the transducer box, with an average element size of 3 mm (Figure 4.8). The geometric order of the acoustic element was linear, i.e. an 8-node linear acoustic brick. The geometric order of stress/displacement element was linear too, which was a four-node linear tetrahedron.

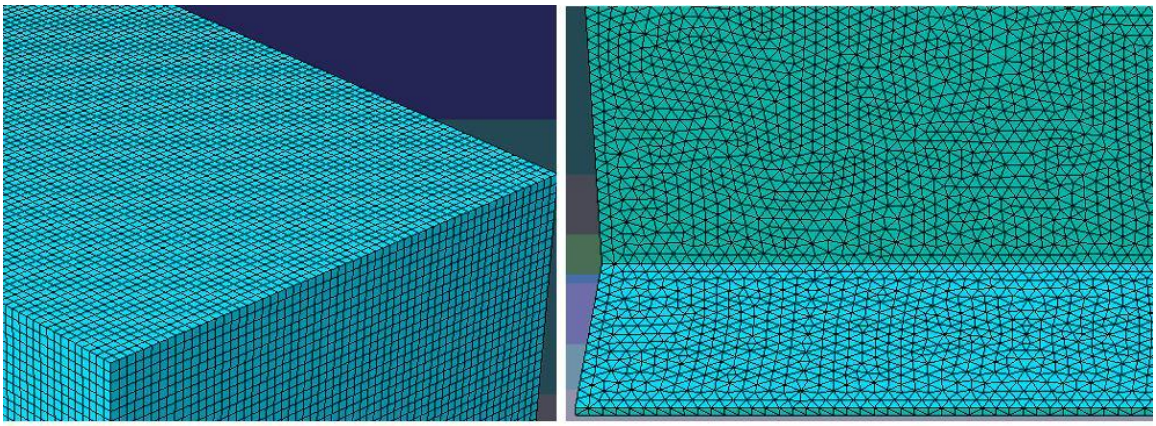

(a) mesh of water (part) (b) mesh of the transducer box (part)

Figure 4.8. Mesh of the washing tank model

4.6. Boundary Conditions

4.6.1 Free Water-air Interface

The are-water interface was set to be a free surface, i.e. p = 0 on the air-water interface. This was based on the fact that the values of the acoustic specific characteristic impedance of air and that of water are in great difference.

The acoustic specific characteristic impedance z is defined as:

(4-13) $$z = \rho c$$

According to this equation, $z_{water} = 1,463,00 \frac{kg}{m^2 \cdot s}$; $z_{air} = 417 \frac{kg}{m^2 \cdot s}$.

The acoustic pressure reflection coefficient at the interface of two media is defined as

(4-14) $$\rho_p = \frac{p_1^r}{p_1} = \frac{z_2 - z_1}{z_2 + z_1}.$$

According to this equation, the pressure reflection coefficient for acoustic waves in water on water-air interface is about -1.0057, which means a nearly 180 degree phase change and equal pressure amplitude for the reflected acoustic wave compared with the incident acoustic wave. By linear superposition, the acoustic pressure on the water-air interface is zero.

4.6.2 Probe-Water Interface

In the model of the sono-reactor, though the transducer probe was not built into the model, all the surfaces of the transducer probe were set to be rigid , i.e. at the walls of the probe, $\frac{\partial p}{\partial n} = 0$, where n is the unit normal vector of the wall. This boundary condition comes from the equation of motion (4-15) for waves propagating in fluid, and the fact that on rigid walls, U = 0.

(4-15) $$-\nabla p = \rho_f \frac{\partial^2 u}{\partial t^2}$$

4.6.3 Non-Reflection Surfaces

In the model of the washing tank, there were three non-reflection surfaces (Figure 4.9). It is because that the water in the washing tank in fact had a huge bulk and it is inefficient to include a large bulk of water in the model. So only water between the two transducer boxes were truncated as the computational region, and water outside that region was cut off. On the three cut surfaces of the water, a non-reflection radiation boundary condition was imposed to allow the acoustic waves to pass through without reflecting back into the computational domain.

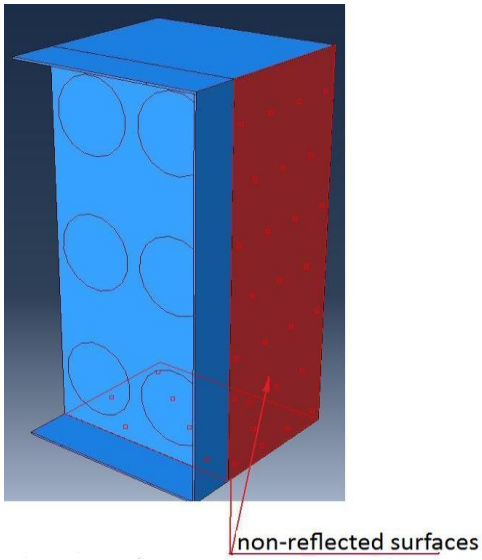

Figure 4.9. Non-reflection surfaces

For radiation boundaries of simple shapes—such as planes, spheres, and ellipses—simple impedance boundary conditions can represent good approximations of the exact radiation conditions. In Abaqus, for steady state, the radiating condition is defined as

(4-16) $$T(X) \equiv -(\frac{i\omega}{c_1} - \frac{\omega^2}{k_1})\tilde{p}.$$

For plane non-reflection surfaces, there is

(4-17) $$\frac{1}{c_1} = \Re(\frac{1}{\sqrt{\tilde{\rho}K_f}}), \text{ and}$$

(4-18) $$\frac{1}{k_1} = \Im(\frac{1}{\omega\sqrt{\tilde{\rho}K_f}}),$$

where $\Re$ represents the real part, $\Im$ represents the imaginary part.

According to equations (4-17) and (4-18), at frequency 20 kHz, $\frac{1}{c_1} = 6,7420 \times 10^{-7}$, $\frac{1}{k_1} = 2.0164 \times 10^{-8}$.

4.6.4 Fixed Areas

For the sonoreactor model, the outer bottom surface of the reactor was set stable, i.e. there was no displace at any direction on that surface. For the washing tank model, areas where the transducer box was fixed onto the frame were set to be stable (Figure 4.10).

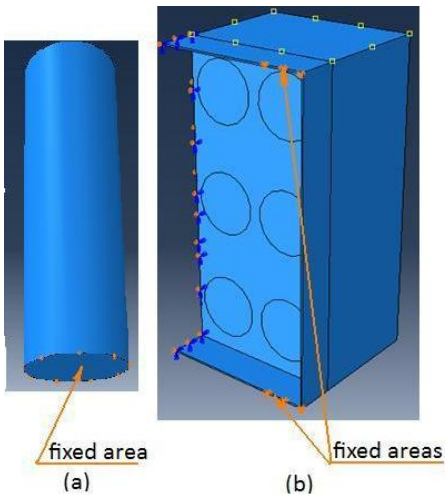

Figure 4.10. Fixed areas: (a) in the sonoreactor model, (b) in the washing tank model

4.7. Constraints

In this simulation, at all the water-solid structure interfaces, surface to surface tie constraints were used in order to include the coupled acoustic-structural effect of water and the solid structure. The surface of the solid structure was set to be a master surface, and the surface of the water was set to be a slave surface. A surface-based tie constraint constrains each of the nodes on the slave surface to have the same motion and the same value of temperature and acoustic pressure as the point on the master surface to which it is closest (Abaqus, 2007). Generally, degrees of freedom common to both surfaces are tied, and any other degrees of freedom are unconstrained.

However, acoustic-structural constraints are exceptions to this rule. Since the relations between the acoustic pressure on the fluid surface and displacements on the solid surface are formed internally. The displacements and/or pressure degrees of freedom on the surfaces are the only ones which are affected by tie constraints; rotations are ignored in this case. In this type of surface-based tie constraint, both the displacement and the pressure of the node on the surface of the solid structure equal to that of the node on the surface of water, correspondingly.

4.8. Load

In acoustics, the “force” conjugated to pressure in the acoustics formulation is the normal pressure gradient at the surface divided by mass density. This comes from the equation of motion for waves propagating in a fluid. The corresponding conjugate force at a node on the surface is the inward volume acceleration, which is the integral of the inward acceleration of the acoustic medium evaluated over the surface area associated with the node (Abaqus, 2007). The inward volume acceleration is dimensionally equal to a force per unit mass.

In the model of the sono-reactor, the acoustic load was applied on water through the tip surface of the probe, changing sinusoidally with time. Since a 12.7 mm diameter probe oscillates with amplitude ranging from 0 to 120 μm, the median amplitude 60 μm was used. The amplitude of the acoustic inward volume acceleration was determined by equation (4-19).

(4-19) $$\ddot{V}_o = \ddot{u}S$$

where $\ddot{u}$ is the acceleration of the fluid particle displacement, which is the same as that of the probe tip. Since $u = 60\times10^{-6}\sin\omega t$, $S = \pi r^2$, where $r = 6.35$ mm is the radius of the probe, V_o is the volume of the medium, $\ddot{V}$ is the acceleration of the volume change.

(4-20) $$\ddot{V}_o = -60\times10^{-6}\times\omega^2\times\pi r^2\sin\omega t \simeq -120.0\sin\omega t\ .$$

In the model of the washing tank, since the mechanical movement of the ultrasound transducer was not applied directly on water, but on the transducer box, so this movement was treated as a sinusoidally changed boundary condition i.e. there was a sinusoidally changed mechanical pressure applied on each area of the transducer box where the ultrasound transducer was attached. The amplitude of this pressure was set to be $1\times10^7\,Pa$.

4.9. Experimental Observations with Aluminum Foils

To map the acoustic field distribution in a sonoreactor or tank, aluminum foils are often used as a non-quantitative method. This is because the measurement of acoustic pressure with hydrophones when cavitation is present is difficult. In the experimental observations, aluminum foils were inserted vertically into the washing tank. The cavitation activities produced by ultrasound pressure will cause pitting or erosion on the foil in regions where the ultrasonic intensities are relatively high. The dimensions of the aluminum foil used were $31\text{cm}\times28\text{cm}$, which was slightly smaller compared to the dimension of the cross-section of the simulation domain ($40\text{cm}\times40\text{cm}$). The aluminum foils were fixed onto a wood frame, inserted in the washing tank, and treated for 30 seconds.

CHAPTER 5 RESULTS AND DISCUSSION

5.1. Acoustic Pressure Distribution in the Sonoreactor

The acoustic pressure distribution in the sonoreactor was simulated by FEM by changing the transducer probe position. Some of the results are shown in Figure 5.1. More simulation results are shown in Figure A.1 in the appendix.

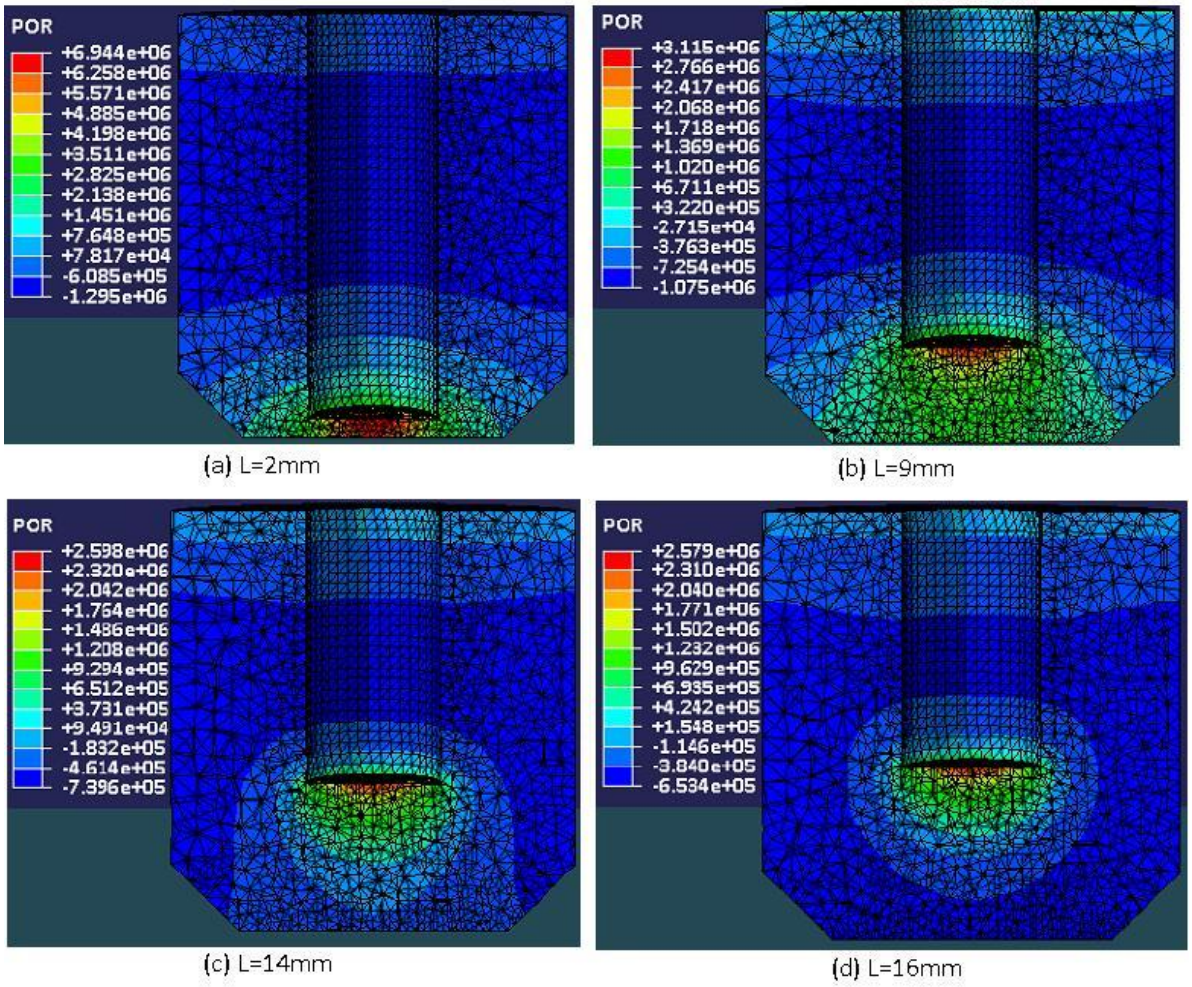

Figure 5.1. Acoustic pressure distribution in the sonoreactor

5.1.1 Pressure Field in the Vicinity of the Probe Tip

It can be seen that the acoustic pressure distribution in the vicinity of the tip of the probe when the distance (L) between the probe tip and the reactor bottom was less than 14 mm was different from that when L was greater than 14 mm, where a similar acoustic pressure distribution in the close vicinity of the probe can be observed (Figures 5.1c and 5.1d).

This is because on one hand, the acoustic pressure decreases quickly as L increases for a "free-field", i.e., the acoustic pressure is distance sensitive when L is small, while being distance insensitive when L is large.

Under the "free-field" conditions, the acoustic pressure along the probe axis decreases following equation 5-1 (Klíma et al., 2007)

(5-1) $$p \approx \sin\frac{k}{2}(\sqrt{x^2 + r^2} - x)$$

where $k = 2\pi / \lambda$ is the wave number, x (or L used in the simulation) is the distance from the probe tip, and r is the radius of the probe. This equation gives a 95% decrease at a distance of $x = 2r$. So at a distance of 13 mm from the tip of the probe, a small change in distance may result in great change in field structure.

On the other hand, since the wave equation used in this simulation is linear, the acoustic pressure field in the sonoreactor can be superposed. It can be viewed as an incident wave field in a free-field plus a mirror symmetric reflection wave field in a free-field (Dähnke et al, 1998), if the fluid viscosity is ignored. When the distance between the probe tip and the sonoreactor bottom is small, both the incident wave field and the reflection wave field are strong, when the distance changes a little, both the incident wave field and the reflection wave field change greatly, so the superposition field changes even bigger. When the distance between the probe tip and the reactor bottom is longer than 13 mm, the pressure structure in the vicinity of the probe tip keeps the form of a semi-sphere.

5.1.2 Pressure Field Near the Reactor Wall

Along the inward normal direction of the reactor wall, the pressure amplitude changes little, i.e. $\frac{\partial p}{\partial n} \approx 0$. It means that the reactor wall with a thickness of 3.2 mm is nearly a rigid boundary for acoustic waves. This agrees with the conclusion of Yasui et al. (2007).

5.1.3 Location of Maximum Acoustic Pressure

The location of the maximum acoustic pressure is at the surface of the probe tip, regardless of the distance between the probe tip and the reactor bottom. This is different from the result reported by Klíma et al. (2007) where the maximum pressure was seen far below the probe. The reasons are as follows.

First, in the work done by Klíma and coworkers, the dissipation of the wave due to fluid viscosity was not considered. The lack of dissipation resulted in that the reflection wave field could be as strong as the incident wave field, and the superposition field would be stronger than the wave source. While when the dissipation of the wave was considered in wave propagation, the reflection wave field will be weaker than the incident wave, and the possibility of the superposition wave field being stronger than the wave source is smaller. Besides, the energy stored in the sonoreactor wall was not included in the simulation done by Klíma and his coworkers, so that all the energy emits by the transducer probe was stored only in the liquid, hence the wave field of their simulation would be stronger than the wave field when the energy consumption by the boundary wall was taken into consideration.

The second and the most important one is that the boundary conditions of the two simulations are of great difference. In this simulation, the reactor was made of stainless steel and the wall was thick and nearly rigid, while in the simulation done by Klíma and coworkers, the reactor was made of glass and the wall was free.

In addition, the distance between the probe tip and the bottom of the reactor also contributes greatly to the differences when comparing the current work with that of Klíma et al.

(2007). The wave length used by two groups is similar, both at about 75 mm. In the simulation of Klíma et al. (2007), the distances between the probe tip and the reactor bottom were all greater than the half wave length 37.5 mm, which allowed the standing wave pattern to be formed, and then the wave pressure antinode stronger than the wave source appeared. While in this simulation the distances between the probe tip and the reactor bottom were all less than the half wave length, which made it impossible for the pressure antinode to be formed.

5.1.4 Relation between the Maximum Acoustic Pressure and the Distance L

L is the distance between the probe tip and the inner surface of the reactor bottom. It is found that although the displacement amplitude (60 μm) of the probe, as well as the volume of the water in the reactor, for each simulation with different L is the same, the maximum acoustic pressure amplitude in each simulation is different. The relation between the simulated maximum pressure amplitude and L is depicted in Figure 5.2.

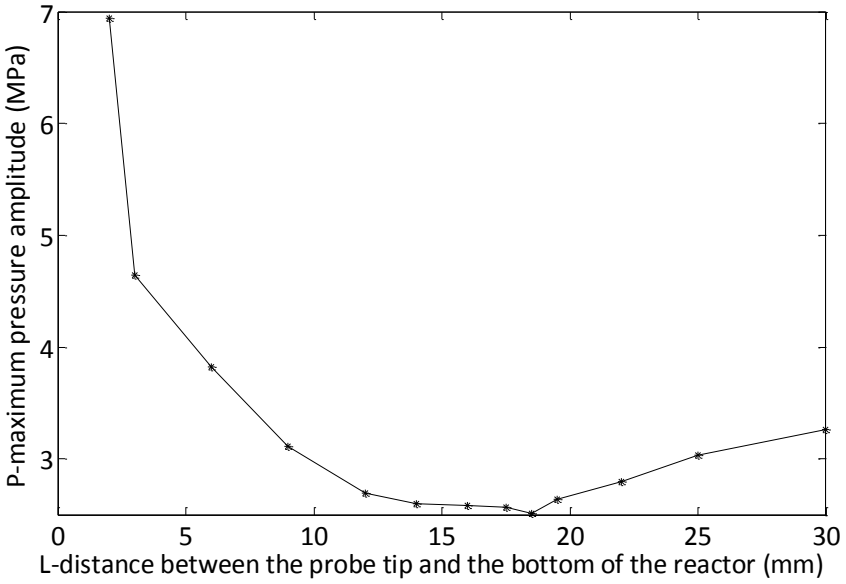

Figure 5.2. Simulated maximum pressure amplitude and L

The smaller L, the higher the maximum pressure amplitude P is. But this rule changes when the distance L is greater than 18.5 mm, which is a wave node. That is because when the distance L is shorter than 18.5 mm, the influence of the water bulk on the pressure field is more important. While when the distance L is longer than 18.5 mm, the influence of the reflected wave on the pressure field becomes more important.

The adiabatic equation of state of a liquid reads

(5-2) $$P = K_{ad} s,$$

where P is the pressure of the liquid; $K_{ad} = 2.2 \times 10^9$ in this simulation is the adiabatic linear bulk modulus of water, s is called condensation, in this simulation, s is defined as:

(5-3) $$s = \Delta\rho / \rho_0 = (\frac{\rho_0 V_b}{V_b - \Delta V_b} - \rho_0) / \rho_0 = \frac{\Delta V_b}{V_b - \Delta V_b},$$

where, ρ_0 is the density of the liquid in equilibrium state. In this simulation, $\Delta V_b = \pi r^2 \times U \approx 7.6006 \times 10^{-9}$ is the volume change of water when the displacement of the probe reaches its maximum, where $r = 0.00635$ m is the radius of the transducer probe, $U = 60 \times 10^{-6}$m is the displacement amplitude of the transducer probe. $V_b = LS$ is the effective volume of water which locates below the transducer probe (Since the volumetric acceleration acts directly on water below the probe, not on water above it), where $S = \pi R^2 \approx 1.1401 \times 10^{-3}$ is the area of the cross section of the reactor, $R = 0.01905$ m is the inner radius of the reactor;

The combination of equations (5-2) and (5-3) yields

(5-4) $$P_{\max} = K_{ad} \frac{\Delta V_b}{LS - \Delta V_b} \approx \frac{16.7213}{1.1401 \times 10^{-3}\text{L} - 7.6006 \times 10^{-9}}.$$

It can be seen from equation (5-4) that, with the same value of ΔV_b, a smaller V_b produces a bigger P. Since $V_b = LS$, and $S \equiv$ cosntant, so a smaller distance L produces a bigger pressure amplitude P. The relationship between the maximum pressure amplitude P and L computed by equation (5-4) is depicted in Figure 5.3.

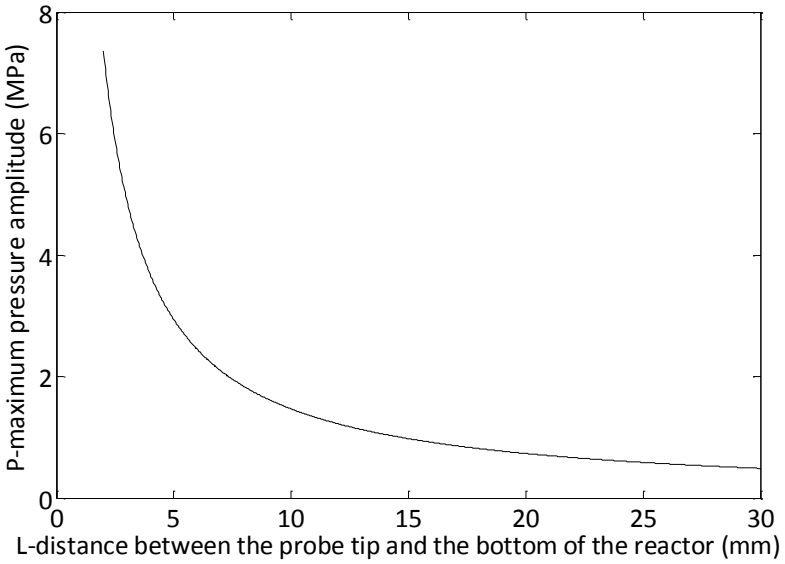

Figure 5.3. Theoretical relationship between P and L

The standing pressure wave equation is as follows:

(5-5) $$P = 2P_{\max} \cos kx \cos \omega t$$

where $k = 2\pi / \lambda$ is the wave number, x is the distance from the reflection plane. The pressure amplitude calculated from equation (5-5) is shown in Figure 5.4.

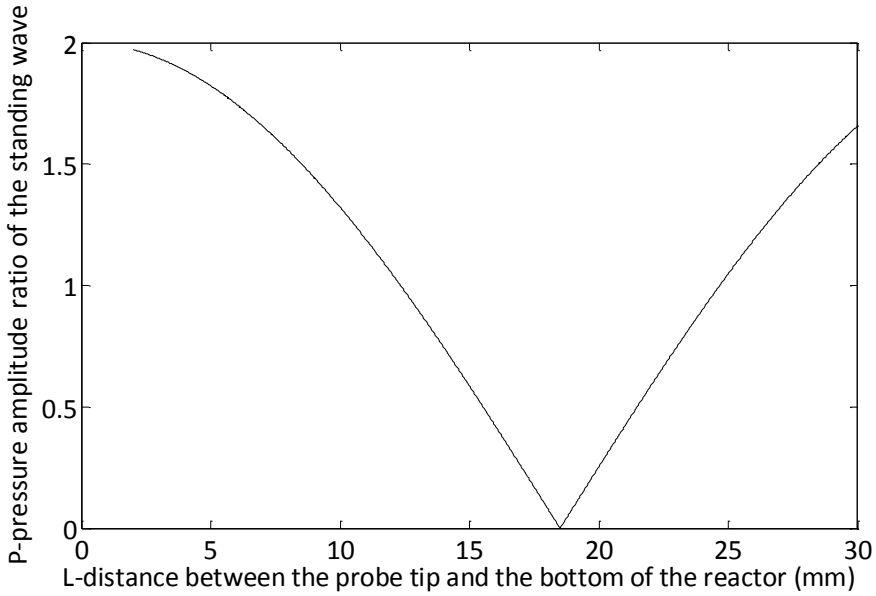

Figure 5.4. Pressure amplitude ratio of the pure standing wave

The combination of equations (5-4) and (5-5) results in the theoretical expression of the maximum pressure amplitude, as a function of the distance L between the probe tip and the reactor bottom.

(5-6) $$P = 2P_{\max}\cos kx = \frac{2\times 16.7213}{1.1401\times 10^{-3}\mathrm{L} - 7.6006\times 10^{-9}}\cos kx$$

The theoretical maximum pressure amplitude calculated from equation (5-6) is shown in Figure 5.5.

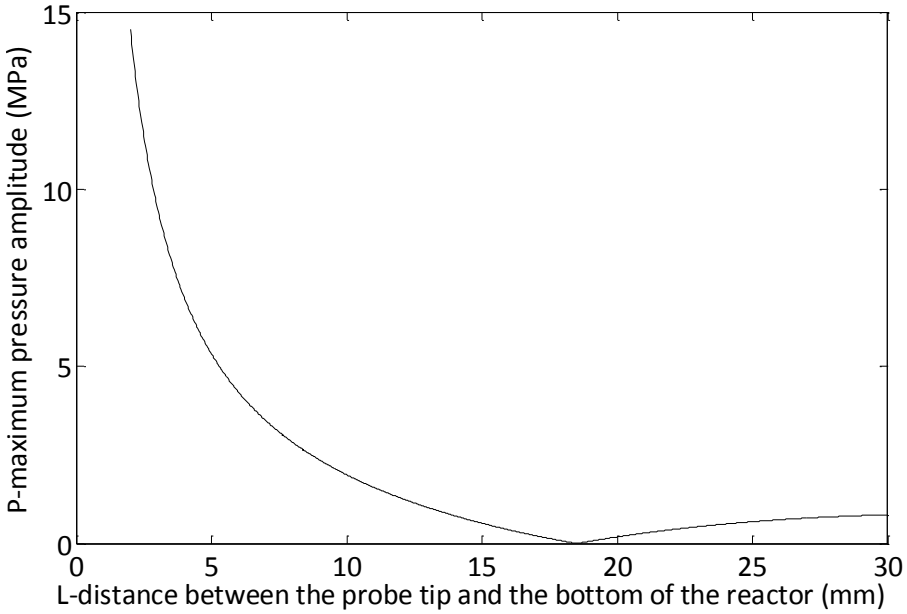

Figure 5.5. Theoretical maximum pressure amplitude and L

By a comparison of Figure 5.2 and Figure 5.5, it can be seen that, the simulation result agrees well with the theoretical one, although the theoretical pressure amplitude is bigger than the simulated pressure amplitude for smaller L and slightly lower for larger L. The location of the only wave pressure node at the distance of $L = \lambda / 4 = 18.5$ mm can be seen in both the simulated result and the theoretical prediction. However, because of the wave attenuation, the pressure at the pressure node was not zero in the simulation.

The reason for theoretical pressure amplitude being bigger than the simulated pressure amplitude for smaller L is that in the simulation, the wave attenuation was counted, in the form

of volumetric drag, while in the theoretical calculation, the attenuation was not considered since it is difficult to get a proper attenuation coefficient. Besides, in the theoretical calculation, as an approximation, the volumetric acceleration was applied only on water below the probe tip, and thus the pressure amplitude is bigger than it is should be by ignoring water above the probe tip.

For the theoretical calculated pressure amplitude, it is smaller than the simulated pressure amplitude for larger L because in the simulation the wave reflection by the reactor wall was considered, while in the theoretical calculation, this reflection was not included.

5.2. Ultrasound Intensity Distribution in the Sonoreactor

The ultrasound intensity distributions in the sonoreactor for selected L values are shown in Figure 5.6. More simulation results can be found in the appendix (Figure A.2). It can be seen that there are areas where the ultrasound intensity is less than 1% of the maximum intensity. These areas are called low intensity areas. For a L of less than 4 mm and greater than 18.5 mm, the low intensity areas have occupied a large portion of the sonoreactor and only at the tip of the probe, relatively high ultrasound intensity can be observed. As a result, the ultrasound intensity distributions in the reactor when L is less than 4 mm and greater than 18.5 mm are not good. If the areas where the ultrasound intensity is greater than 5% of the maximum intensity are considered, for L=14 mm, the ultrasound intensity distribution is improved, while for L = 12 mm, the intensity distribution is better, for L = 6 mm and L = 9 mm, the intensity distributions are further improved.

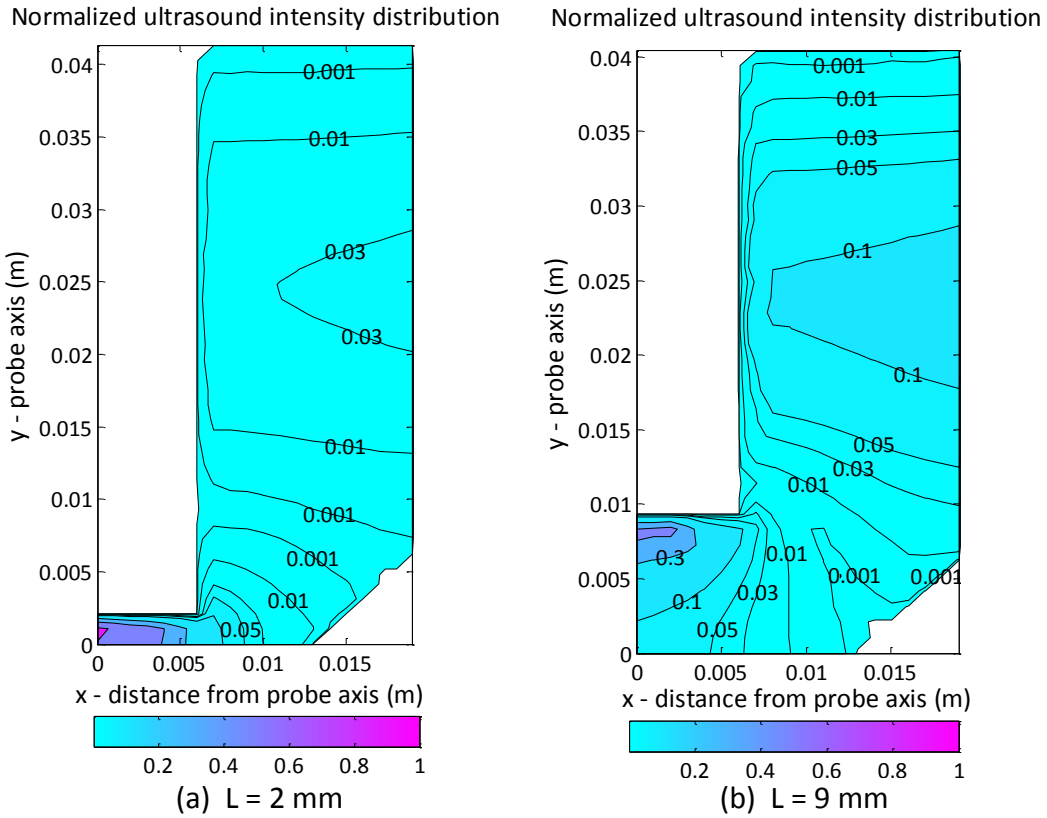

Figure 5.6. Normalized ultrasound intensity distributions in the reactor

For L = 9 mm, there is a big area where the ultrasound intensity is more than 10% of the maximum value. This is the best intensity distribution among the L values simulated.

Two decontamination experiments were performed for L = 2 mm and L = 14 mm, and the results are shown in Figure 5.7. It can be seen that the reduction in the survival count of *E. coli* K12 cells in the two chambers is significantly different. A relatively rapid reduction was achieved for the chamber B with L = 14 mm, as compared to that in Chamber A with L = 2 mm. From the situation shown in Figure 5.6, the ultrasound intensity distribution in the L = 2 mm vessel was much less uniform than that in the L = 14 mm vessel. This inactivation test serves as a good indication of the correctness of the simulation produced in this study.

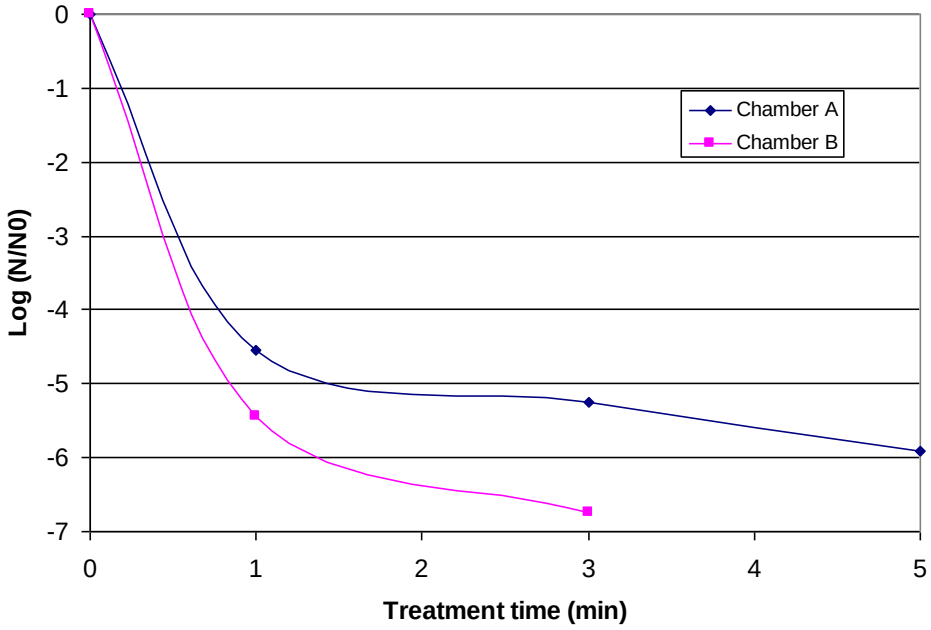

Figure 5.7. Survival curve of *E. coli* K12 in phosphate buffer (0.01 M, pH 7) treated by batch mano-thermo-sonication in Chamber A (L = 2 mm) and B (L = 14 mm) at 60°C and 400 kPa.

5.3. Acoustic Pressure Distribution in the Washing Tank

The simulated ultrasound pressure distributions and experimental observations of the pressure distributions obtained in aluminum foil tests in the washing tank at cross-section of Z = 12 cm, Z = 5 cm, Z = 0 cm and X = -20 cm are shown in Figure 5.8, where Z was the coordinate of the cross-section parallel to X-Y plane, X was the coordinate of the cross-section parallel to Y-Z plane (see Figure 5.9 for the coordinate system). In the experimental observations, aluminum foils were inserted in the washing tank at locations described above and eroded in the regions where relatively high ultrasound pressure produced high cavitation activities. The dimensions of the aluminum foil used were $31\text{cm} \times 28\text{cm}$, smaller than the dimensions of the cross-section of the simulation domain. It can be seen that the simulated ultrasound field distribution agrees well with erosion patterns on the aluminum foils.

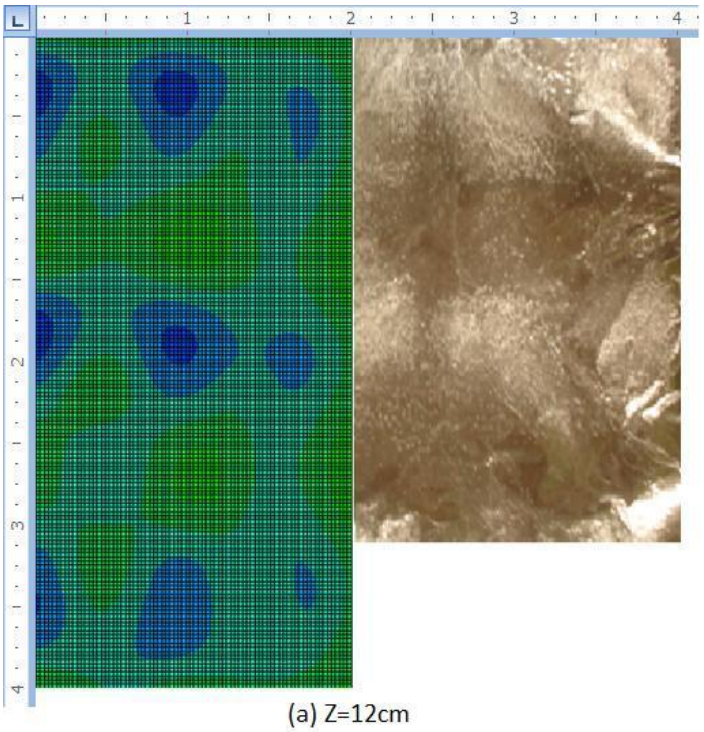

(a) Z=12cm

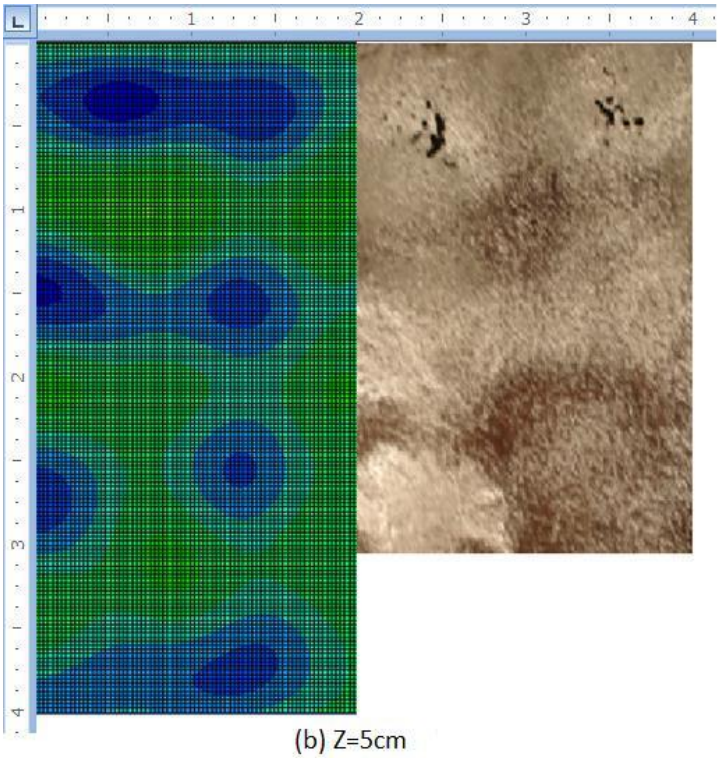

(b) Z=5cm

Figure 5.8. Ultrasound pressure distributions in the washing tank

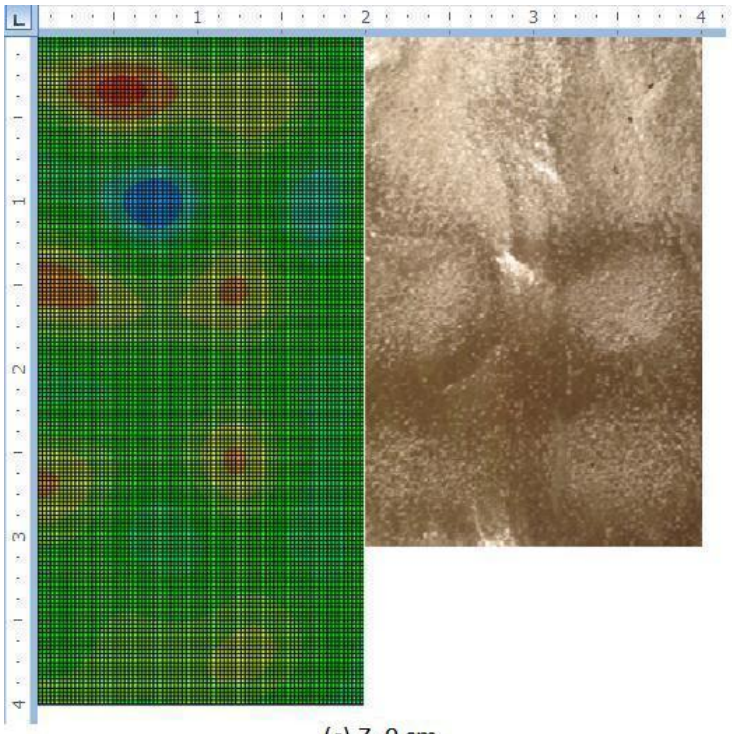

(c) Z=0 cm

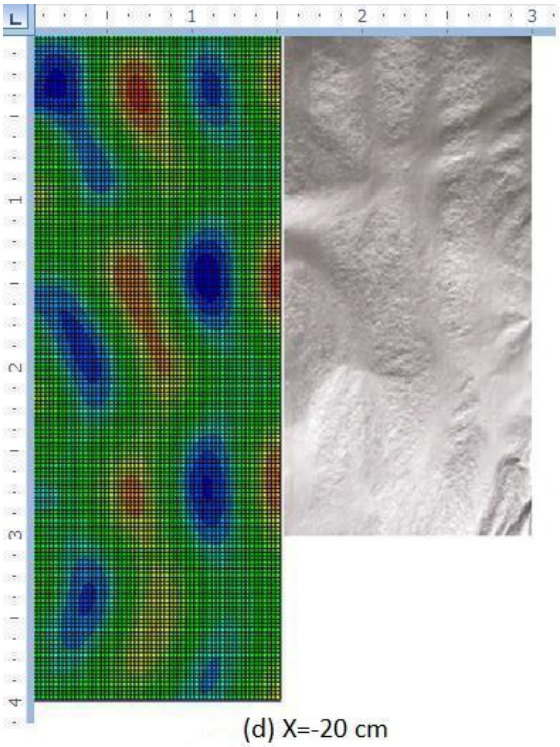

(d) X=-20 cm

Figure 5.8. Ultrasound pressure distributions in the washing tank (cont.)

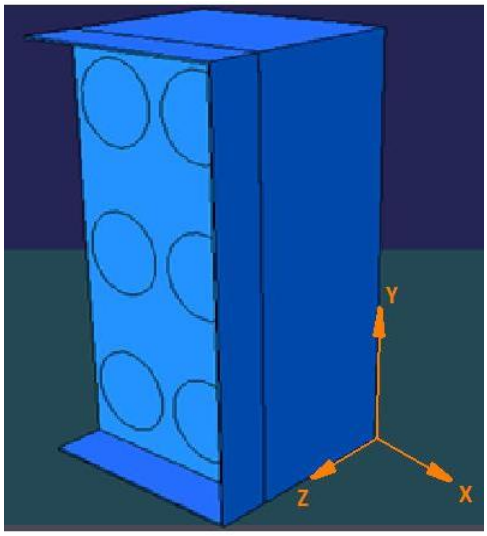

Figure 5.9. The coordinate system of the washing tank model

At Z = 12 cm, the simulated ultrasound pressure distribution pattern clearly shows the location of the transducers. The pressure amplitude was high where the transducer locates. This is because at a distance of Z = 12 cm which was 3 cm from the transducer emitting surface, the ultrasound energy had not been dissipated or spread.

The pressure amplitude was low near the edge of the transducer box as can be seen from all the simulation results. This is because the stiffness at the edge of the box was large, which led to a small vibration amplitude near the edge of the transducer box. The pressure field between the transducers was small too. The reason is that the oscillating driving force there was smaller than where the transducers are located.

The pressure field at the upper half of the cross-section (near the water-air interface) was stronger than the pressure field in the lower part of the cross section. This can be attributed to the fact that for the upper part of the cross section, there was a total wave reflection from above--the water-air interface, so the pressure field there was in fact doubled. While in the lower part of the cross section, the wave field spread out. There was no strong reflected wave field from below, except for the wave reflected by the water-air interface, which had traveled a relatively longer distance and attenuated.

Since the superposition of multiple wave sources (multiple transducers) was complex, the numbers of the wave antinodes in cross-sections of Z = 5 cm and Z = 0 cm were more than the number of the transducers.

On the cross-section parallel to Y-Z plane, at the middle of the transducer box, the simulated ultrasound field is shown in Figure 5.9(d). There was standing wave pattern in the ultrasound pressure distribution, which agrees well with the erosion effect of aluminum foils. This characteristic was also verified by the work done by Ando and Kagawa (1989).

The largest ultrasound pressure amplitude in water was 1.397×10^{7} Pa, located on the cross-section Z=15 cm. This pressure amplitude was slightly greater than the applied pressure amplitude 1×10^{7} Pa. This could be caused by in the linear superposition of the ultrasound fields radiating from two transducer boxes and the reflections.

CHAPTER 6 CONCLUSIONS

The ultrasound pressures distribution in the sonoreactor with a fixed volume of water at different L values, which was the distance between the tip of the ultrasound probe and the bottom of the reactor inner wall, was simulated by using finite element method (FEM) via Abaqus, by taking into account the coupling effect between the sonoreactor wall and the ultrasound medium. The ultrasound intensity distribution was then calculated based on the acoustic pressure distribution obtained from the simulation. The optimal position of the ultrasonic probe along the axis of the sonoreactor was where L=9 mm. The validity of the computer simulation was evaluated by comparing the ultrasound intensity distributions in the sonoreactor at two different L values with the result of a microbial inactivation test conducted in the same sonoreactor for each L value when treated by mano-thermo-sonication in a batch operation.

The simulated acoustic pressure field between two transducer boxes in a custom-made ultrasound-assisted washing tank was computed and compared with the result of erosion tests with aluminum foils. A relatively good agreement was achieved between the FEM simulation and the pitting patterns formed on the aluminum foils caused by cavitation activities. With the current design of the ultrasound-assisted washing tank, both the simulation and erosion test showed that the ultrasound field distribution between two transducer boxes in the washing tank was relatively uniform. The FEM models developed in this study can be used to assist the design and optimization of ultrasound treatment chambers.

CHAPTER 7 FUTURE WORK

In the simulation conducted in this study, the energy absorption of the solid structures was not analyzed. The effect of the solid structures on the acoustic field distribution in the sonoreactor or ultrasonic tank will be examined in future studies in order to analyze the energy consumed in cavitation.

In the simulation of the ultrasound field distribution in the washing tank, the transducers were not included in the analysis domain. Instead, a distributed pressure boundary condition was applied. Since the transducers were attached onto the inner surfaces of the transducer box, and vibrate at the same time, a simulation includes the transducers should be more appropriate.

In the simulation of the washing tank, the vibration of the tank wall was ignored. While in fact, a complicated system like the washing tank should have several resonant frequencies with which the same energy input would result in a much stronger cavitation result. The determination of the resonant frequencies of the system should be another important component for future investigations.

REFERENCES

Abaqus. 2007. *Abaqus Theory Manual* . Ver. 6.7. Norhtville, MI.: Dassault Systèmes.

AFF. *Alliance for Food and Farming*. 2010. http://www.foodandfarming.info/docs/386Produce_Analysis_2010_Final.pdf (accessed May 1, 2011).

Allende, A., F.A. Tomás-Barberan and M.I. Gil. 2006. Minimal processing for healthy traditional foods. *Trends in Food Science & Technology* 17(9): 513-519.

Alterkrus, S.F., M.L. Cohen, and D.L. Swerdlow. 1997. Emerging food borne diseases. *Emerging Infectious Diseases* 3: 285-293.

Ando, E. and Y. Kagawa. 1989. Finite element simulation for the design of an ultrasonic cleaning tank. *Electronic and communications in Japan*, Part 3, 72 (7): 1079-1090.

Apfel, R.E. 1981. Ultrsonics. In *Methods of Experimental Physic* 19: 356-411. P.D. Edmonds, ed. New York: Academic Press.

Ashurst, P.R. 2007. Fruit Juices. In *Kirk-Othmer Encyclopedia of Chemical Technology*, 1-22. http://onlinelibrary.wiley.com.proxy2.library.illinois.edu/doi/10.1002/0471238961.0618210919080123.a01.pub2/pdf. (accessed April 30, 2011)

Baumann, A.R., S.E. Martin, and H. Feng. 2005. Power ultrasound treatment of Listeria monocytogenes in apple cider. *Journal of Food Protection* 68(11): 2333-2340.

Berrang, M.E., J.F. Frank, and R.J. Meinersmann. 2008. Effect of Chemical Sanitizers with and without Ultrasonication on Listeria monocytogenes as a Biofilm within Polyvinyl Chloride Drain Pipes. *Journal of Food Protection* 71(1): 66-69.

Beuchat, L.R. 1996. Listeria monocytogenes: incidence on vegetables. *Food Control* 7:223-228.

Beuchat, L.R. 1998. Surface Decontamination of Fruits and Vegetables Eaten Raw: A Review. *World Health Organization Publication* No. WHO/FSF/FOS/98.2. World Health Organization.

Beuchat, L.R. 2004. Difficulties in eliminating human pathogenic microorganisms on raw fruits and vegetables. *Acta Horiculturae* (ISHS) 642: 151-160.

Bretz, N., J. Strobel, M. Kaltenbacher and R. Lerch. 2005. Numerical simulation of ultrasonic waves in cavitation fluids with special consideration of ultrasonic cleaning. *2005 IEEE Ultrasonics Symposium* 1: 703-706.

Butz, P. and B. Tauscher. 2002. Emerging technologies: chemical aspects. *Food Research International* 35(2-3): 279-284.

Carmichael, I., Harper, I.S., Coventry, P.M.J. Taylor, J. Wan and, M.W. Hickey 1999. Bacterial colonization and biofilm development on minimally processed vegetables. *Journal of Applied Microbiology* 85(S1): 45S-51S.

CDC. *Centers for Disease Control and Prevention*. 1997. Outbreaks of Escherichia coli O157:H7 Infection and Cryptosporidiosis Associated with Drinking Unpasteurized Apple Cider—Connecticut and New York, Octorbor 1996. *Morbidity and Mortality Weekly Report* 46(01): 4-8.

CDC. *Centers for Disease Control and Prevention*. 2006. Surveillance for Foodborne-Disease Outbreaks -- United States, 1998--2002. *Morbidity and Mortality Weekly Report* 55(SS-10):1-34.

CDC. *Centers for Disease Control and Prevention*. 2009. Surveillance for Foodborne-Disease Outbreaks -- United States, 2006. *Morbidity and Mortality Weekly Report* 58(22):609-615.

CTG. *Cleaning Technologies Group*. 2009. http://www.ctgclean.com/technology-library/articles/magnetostrictive-versus-piezoelectric-transducers-for-power-ultrasonic-applications/ (accessed April 01,2011)

Dähnke, S.W. and F.J. Keil. 1998. Modeling of three-dimensional linear pressure fields in sonochemical reactors with homogeneous and inhomogeneous density distribution of caviation bubbles. *Industrial & Engineering Chemistry Research* 37(3): 848-864.

Dähnke, S.W., K.M. Swamy, and F.J. Keil. 1999. Modeling of three-dimensional pressure fields in sonochemical reactors with an inhomogeneous density distribution of caviation bubbles. Comparison of theorectical and experimental results. *Ultrasonics Sonochemistry* 6(1-2): 31-41.

Demirdoven, A. and T. Baysal. 2009. The use of ultrasound and combined technologies in food preservation. *Food Reviews International* 25(1): 1-11.

De Roever, C. 1998. Microbiological safety evaluations and recommendations on fresh produce. *Food Control* 9(5): 321-347.

Earnshaw, R.G., J. Appleyard, and R.M. Hurst. 1995. Understanding physical inactivation processes: combined preservation opportunities using heat, ultrasound and pressure. *International Journal of Food Microbiology* 28(2): 197-219.

Fahy, F. 2001. *Foundations of Engineering Acoustics.* London, UK. AP Press.

Fellows, P., 2000. *Food Processing Technology: Principles and Practice*. 2nd ed. New York: CRC Press.

Feng, H. and W. Yang. 2006. Chapter 121: Power ultrasound. In *Handbook of Food Science, Technology and Engineering* 3:1-7. H.Y.Hui, ed. Boca Raton, FL.: CRC Press.

Flint, E.B. and K.S. Suslick. 1991. The temperature of cavitation. *Science* 253: 1397–1398.

FDA. *Food and Drug Administration*. 1998a. Food Safety Hazards for Fresh Fruits and Vegetables. http://www.fda.gov/downloads/Food/GuidanceComplianceRegulatoryInformation/GuidanceDocuments/ProduceandPlanProducts/UCM169112.pdf. (accessed May 2,2011)

FDA. *Food and Drug Administration*. 1998b. Hazard analysis and critical control point (HACCP); procedures for the safe and sanitary processing and importing of juice; food labeling; warning and notice statements; labeling of juice products; final rules. *Federal Register* 63:37029-37056.

Gandhi, M., Golding, S., Yaron, S. and Mattews, K.R. 2001. Use of green fluorescent protein expressing Salmonella Stanley to investigate survival, spatial loction, and control of alfalfa sprouts. *Journal of Food Protection* 64:1891-1898.

Gil, M.I., M.V. Selma, F. Lopez-Galvez, A. Allende. 2009. Fresh-cut product sanitation and wash water disinfection: problems and solutions. *International Journal of Food Microbiology* 134(1-2):37-45.

Gogate, P.R., A.M. Wilhelm, and A.B. Pandit. 2003. Some aspects of the design of sonochemical reactors. *Ultrasonics Sonochemistry* 10(6): 325–330.

Harvey, E. N., and Loomis, A L. 1929. The destruction of luminous bacteria by high frequency sound waves. *Journal of Bacteriology* 17: 373-376.

Herdt, J. and H. Feng. 2009 Aqueous antimicrobial treatments to improve fresh and fresh-cut produce safety. In *Microbial Safety of Fresh Produce: Challenges, Persepectives and Strategies,* 169-190. X. Fan, B.A. Niemira, C.J. Doona, F. Feeherry, R.B. Gravani, ed. Ames, Iowa: Wiley-Blackwell.

Huang, T.-S., C. Xu, K. Walker, P. West, S. Zhang, and J. Weese. 2006. Decontamination efficacy of combined chlorine dioxide with ultrasonication on apples and lettuce. *Journal of Food Science* 71(4): M134-M139.

Hunter, G., M. Lucas, I. Watson, and R. Parton. 2008. A radial mode ultrasonic horn for the inactivation of *Escherichia coli* K12. *Ultrasonics Sonochemistry* 15(2): 101-109.

Jenderka, K.-V. and C. Koch. 2006. Investigation of spatial distribution of sound field parameters in ultrasound cleaning baths under the influence of cavitation. *Ultrasonics* 44(supplement): e401-e406.

Kim, K.Y., K.-T. Byun, H.-Y. Kwak. 2007. Temperature and pressure fields due to collapsing bubble under ultrasound. *Chemical Engineering Journal* 132(1-3):125-135.

Klíma, J., A. Frias-Ferrer, J. González-García, J. Ludvík, V. Sáez and J. Iniesta. 2007. Optimisation of 20 kHz sonoreactor geometry on the basis of numerical simulation of local ultrasonic intensity and qualitative comparison with experimental results. *Ultrasonics Sonochemistry* 14(1): 19-28.

Komarov, S.V., M. Kuwabara and O.V. Abramov. 2005. High power ultrasonics in pyromettallurgy: current status and recent development. *ISIJ International* 45(12): 1765-1782.

Lee, H., B. Zhou, H. Feng, and S.E. Martin. 2009b. Effect of pH on inactive of Escherichia coli K12 by sonication, manosonication, thermosonication, and manothermosonication. *Journal of Food Science* 74(4): E191-E198.

Lee, H., B. Zhou, W. Liang, H. Feng, and S.E. Martin. 2009a. Inactivation of *Escherichia col*i cells with sonication, manosonication, thermosonication and manothermosonication: Microbial responses and Kinetics modeling. *Journal of Food Engineering* 93(3): 354-364.

Leighton, T.G. 1994. *The Acoustic Bubble.* San Diego: Academic Press.

Leighton, T.G. 1998. The principles of cavitation. In *Ultrsound in food processing*, 151-178. M.J.W. Povey, & T.J. Mason, eds. London, UK.: Blackie Academic & Professional.

Lin, S. and F. Zhang. 2000. Measurement of ultrasonic power and electro-acoustic efficiency of high power transducers. *Ultrasonics* 37(8): 549-554.

Lorimer, J.P. and T.J. Mason. 1987. Sonochemistry part 1—the physical aspects. *Chemical Society Reviews* 16: 239-274.

Louisnar, O., J. Gonzalez-Garcia, I. Tudela, J. Klima, V. Saez, and Y. Vargas-Hernande. 2009. FEM simulation of a sono-reactor accounting for vibrations of the boundaries. *Ultrasonics Sonochemistry* 16(2): 250-259.

Lynch, M., J. Painter, R. Woodruff and C. Braden. 2006. Surveillance for food disease outbreaks—United States, 1998-2002. *Morbidity and Mortality Weekly Report* 55(SS10): 1-34.

Marangopoulos, I.P., C.J. Martin, and J.M.S. Hutchsion. 1995. Measurement of field distributions in ultrasonic cleaning baths: implications for cleaning efficiency. *Physics in Medicine and Biology* 40(11): 1897-1908.

Martin, C.J. and A.N.R. Law. 1980. The use of thermistor probes to measure energy distribution in ultrasound fields. *Ultrasonics* 18(3): 127-133.

Mason, T.J. 2003. Sonochemistry and sonoprocessing: the link, the trends and (probably) the future. *Ultrasonics Sonochemistry* 10(4-5): 175-179.

Mason, T.J., and J.P. Lorimer. 2002. *Applied Sonochemistry.* Weinheim, Germany: Wiley-VCH.

Mead, E.L, R.G. Sutherland, and R.E. Veerrall. 1976. The effect of ultrasound on water in the presence of dissolved gases. *Canadian Journal of Chemistry* 54(7):1114-1120.

Mott, I.E.C., D.J. Stickler, W.T. Coakley, and T.R. Bott. 1998. The removal of bacterial biofilm from water-filled tubes using axially propagated ultrasound. *Journal of Applied Microbiology* 84(4): 509–514.

O'Donnell, C.P., B.K. Tiwari, P. Bourke and P.J. Cullen. 2010. Effect of ultrasonic processing on food enzyme of industrial importance. *Trends in Food Science & Technology* 21(7): 358-367.

Olsen, S.J., L.C. MacKinon, J.S. Goulding, N.H. Bean, and L. Slutsker. 2000. Surveillance for food disease outbreaks—United States, 1993-1997. *Morbidity and Mortality Weekly Report*. 49(SS01): 1-51.

Pan, J., X.-X. Xia, and J. Liang. 2008. Analysis of pesticide multi-residues in leafy vegetables by ultrasonic solvent extraction and liquid chromatography-tandem mass spectrometry. *Ultrasonics Sonochemistry* 15(1): 25–32.

Parish, M.E. 1997. Public health and nonpasteurized fruit juices. *Critical Reviews in Microbiology* 23(2): 109- 119.

Piyasena, P., E. Mohareb, and R.C. McKellar. 2003. Inactivation of microbes using ultrasound: a review. *International Journal of Food Microbiology* 87(3): 207-216.

Povey, J.W. and T. Mason. 1998. Ultrasound in food processing. London, Weinheim, New York, Tokyo, Melburne, Madras: Blackie Academic & Professional

Rae, J., M. Ashokkumar, O. Eulaerts, C.V. Sonntag, J. Reisse, and F. Grieser. 2005. Estimation of ultrasound induced cavitation bubble temperatures in aqueous solutions. *Ultrasonics Sonochemistry* 12(5): 325-329.

Raviyan, P., Z. Zhang, and H. Feng. 2005. Ultrasonication for tomato pectinmethylesterase inactivation: effect of cavitation intensity and temperature on inactivation. *Journal of Food Engineering* 70(2): 189-196.

Rodgers, S.L. and E.T. Ryster. 2004. Reduction of microbial pathogens during apple cider production using sodium hypochlorite, copper ion, and sonication. *Journal of Food Protection* 67(4):767-771.

Sapers G.M. 1998. New techniques for safer produce—chemical-based treatments and decontamination by washing. In: *Proceedings of the 4th Annual Symposium on Food Safety in the 21st Century—fresh fruits and vegetables: food safety challenges*. Chicago, IL.: Center of Food Safety and Continuing Education Committee of the Institute of Food Technologists.

Sapers, G.M., R.L. Miller, and A.M. Mattrzzo. 1999. Effectiveness of sanitizing agents in inactivating *Escherichai coli* on Golden Delicious apples. *Journal of Food Science* 64(4):734-737.

Sáez, V., A. Frías-Ferrer, J. Iniesta, J. González-García, A. Aldaz, and E. Riera. 2005. Chacterization of a 20 kHz sonoreactor. Part I: analysis of mechanical effects by classical and numerical methods. *Ultrasonic Sonochemistry* 12(1-2): 59-65.

Save, S.S., A.B. Pandit, and J.B. Joshi. 1997. Use of hydrodynamic cavitation for large scale microbial cell disruption. *Food and Bioproducts Processing* 75(1): 41-49.

SCCU. *The Sonochemistry Center at Coventry University*.2007. http://www.sonochemistry.info/introdution.htm (accessed May 01, 2011).

Scouten, S.J., and L.R. Beuchat. 2002. Combined effects of chemical, heat and ultrasound treatments to kill Salmonella and Escherichia coli O157:H7 on alfalfa seeds. *Journal of Applied Microbiology* 92(4): 668-674.

Seymour, I.J., D. Burfoot, R. L. Smith, L. A. Cox, and A. Lockwood. 2002. Ultrasound decontamination of minimally processed fruits and vegetables. *International Journal of Food Science and Technology* 37(5): 547-557.

Shutilov, V.A. 1988. *Fundamental Physics of Ultrasound*. London, UK.: Gordon and Breach Science Pulbishers.

Soria, A.C. and M. Villamiel. 2010. Effect of ultrasound on the technological properties and bioactivity of food: a review. *Trends in Food Science and Technology* 21(7): 323-331.

Suslick, K.S. 1986. Oranometallic sonochemistry. *Advances in Organometallic Chemistry* 25: 73-119.

Tsukamoto, I., B. Yim, C.E. Stavarache, M. Furuta, K. Hashiba, and Y. Maeda. 2004. Inactivation of Saccharomyces cerevisiae by ultrasonic irradiation. *Ultrasonics Sonochemistry* 11(2):61-65.

Ugarte-Romero, E., H. Feng and S. E. martin. Inactivation of *Shigella boydii* 18 IDPH and *Listeria monocytogenes* Scott A with power ultrasound at different acoustic energy densities and temperatures. 2007. *Journal of Food Science* 72(4): M103-M107.

Ugarte-Romero, E., H. Feng, S.E. martin, K.R. Cadwallader, and S.J. Robinson. Inactivation of *Escherichia coli* with power ultrasound in apple cider. 2006. *Journal of Food Science* 71(2): E102-E108.

Venkitanarayanan, K. S., C.-M. Lin, H. Bailey, and M.P. Doyle. Inactivation of *Escherichia coli* O157:H7, *Salmonella enteritidis*, and *Listeria monocytogenes* on apples, oranges, and tomatoes by lactic acid with hydrogen peroxide. 2002. *Journal of Food Protection* 65(1): 100-105.

Wiley, R.C. 1994. *Minimally processed refrigerated fruits and vegetables*. London, UK: Chapman & Hall.

Xu, J., X. Ren, W. Gong, R. Dai, and D. Liu. 2003. Measurement of the bulk viscosity of liquid by Brillouin scattering. *Applied Optics* 42(33): 6704-6709.

Yasui, K., T. Kozuka, T. Tuziuti, A. Towata, Y. Iida, J. King, and P. Macey. 2007. FEM calculation of an acoustic field in a sonochemical reactor. *Ultrasonics Sonochemistry* 14(5): 605-614.

Zhou, B., H. Feng, and Y. Luo. 2009. Ultrasound enhanced sanitizer efficacy in reduction of Escherichia coli O157:H7 population on spinach leaves. *Journal of Food Science* 74(6): M308-M313.

APPENDIX

Table A.1. Distance L and water height H

L (mm)	H (mm)
2	41.3
4	41.1
6	40.8
8	40.6
10	40.3
12	40.1
14	39.8
16	39.6
17.5	39.4
18.45	39.3
19.5	39.1
22	38.8
25	38.5
27	38.2

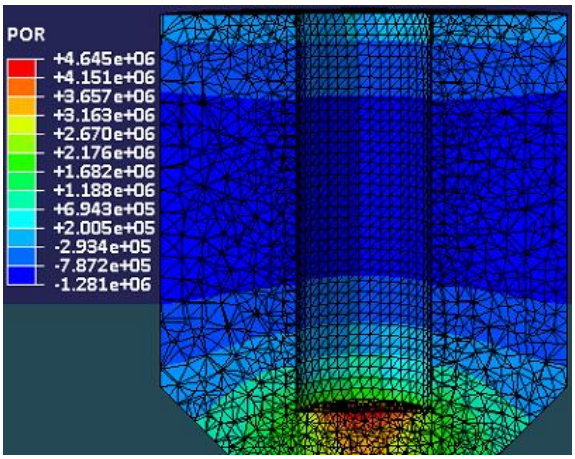

(a) L = 4 mm

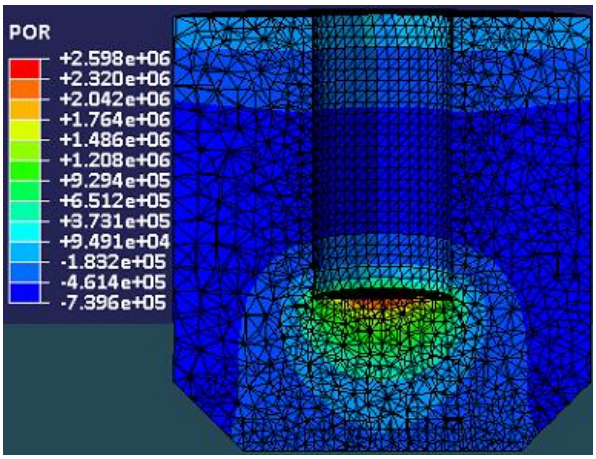

(d) L = 14 mm

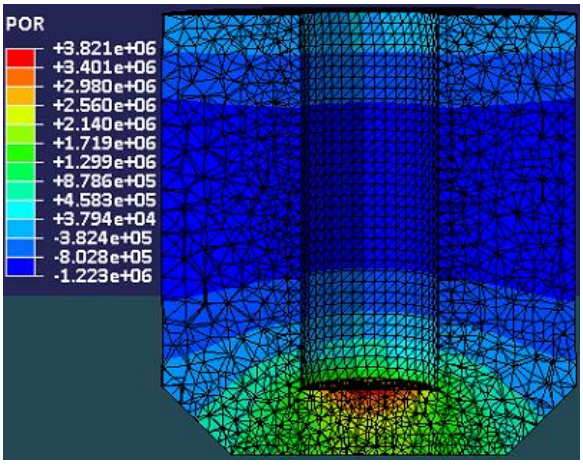

(b) L = 6 mm

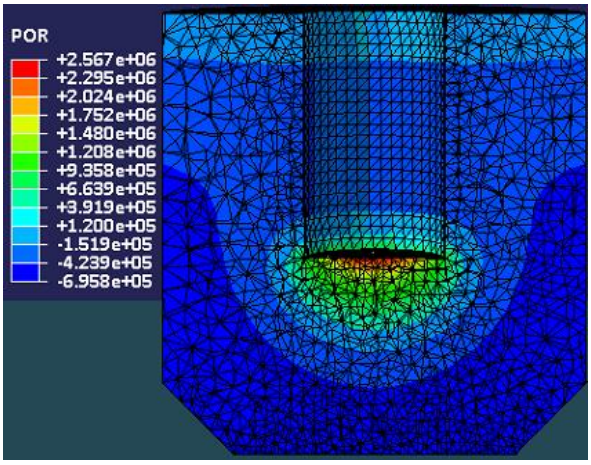

(e) L = 17.5 mm

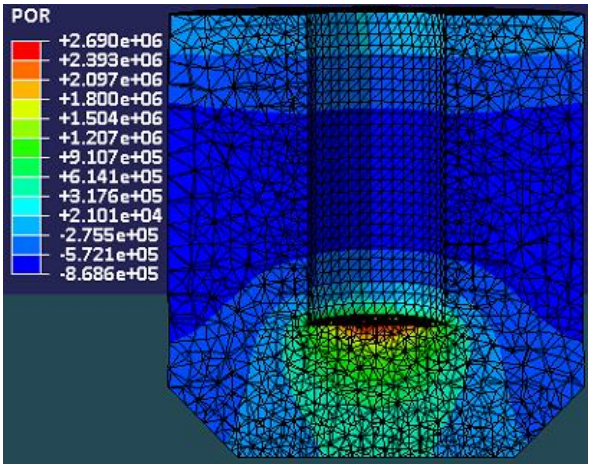

(c) L = 12 mm

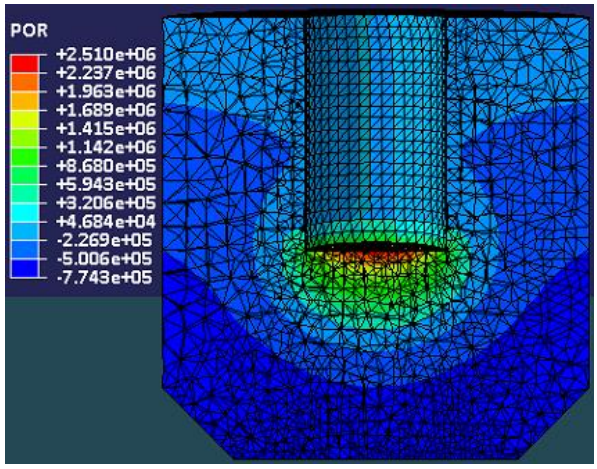

(f) L = 18.5 mm

Figure A.1. Acoustic pressure distribution in the sonoreactor

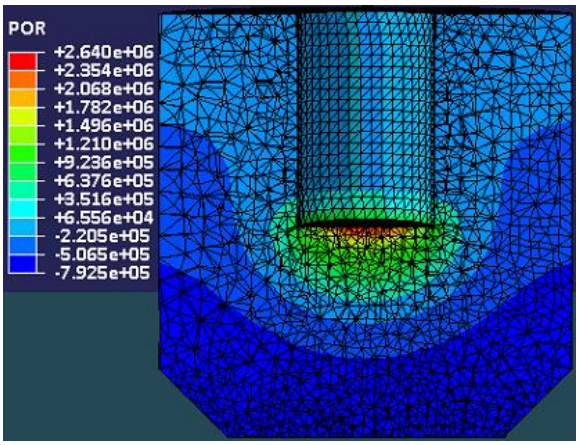

(g) L = 19.5 mm

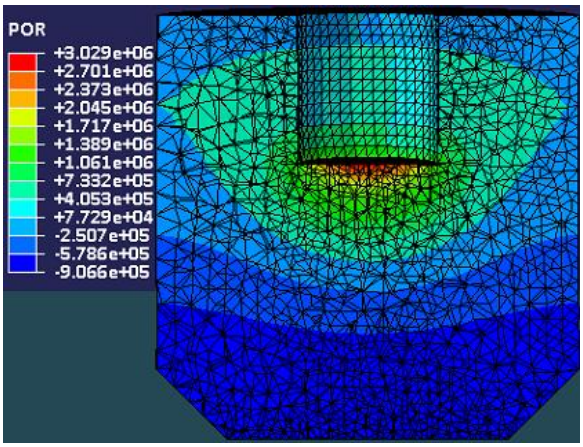

(j) L = 27 mm

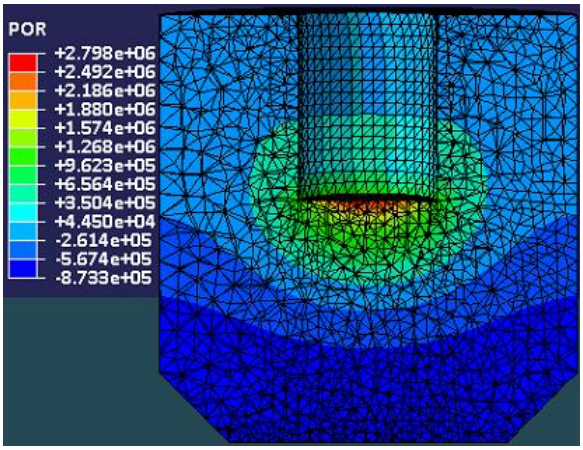

(h) L = 22 mm

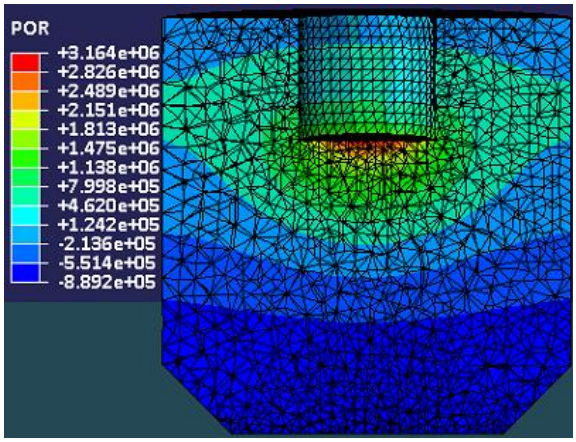

(k) L = 30 mm

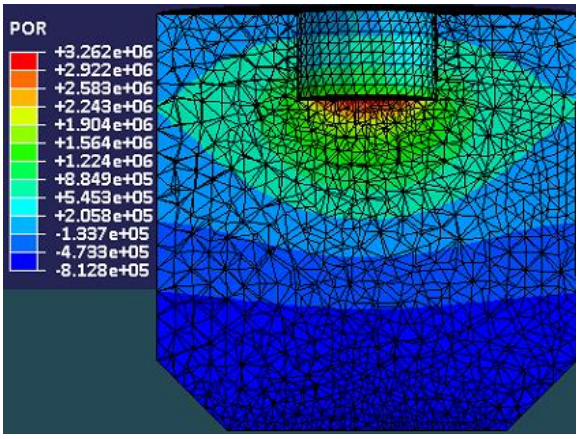

(i) L = 25 mm

Figure A.1. Acoustic pressure distribution in the sonoreactor (cont.)

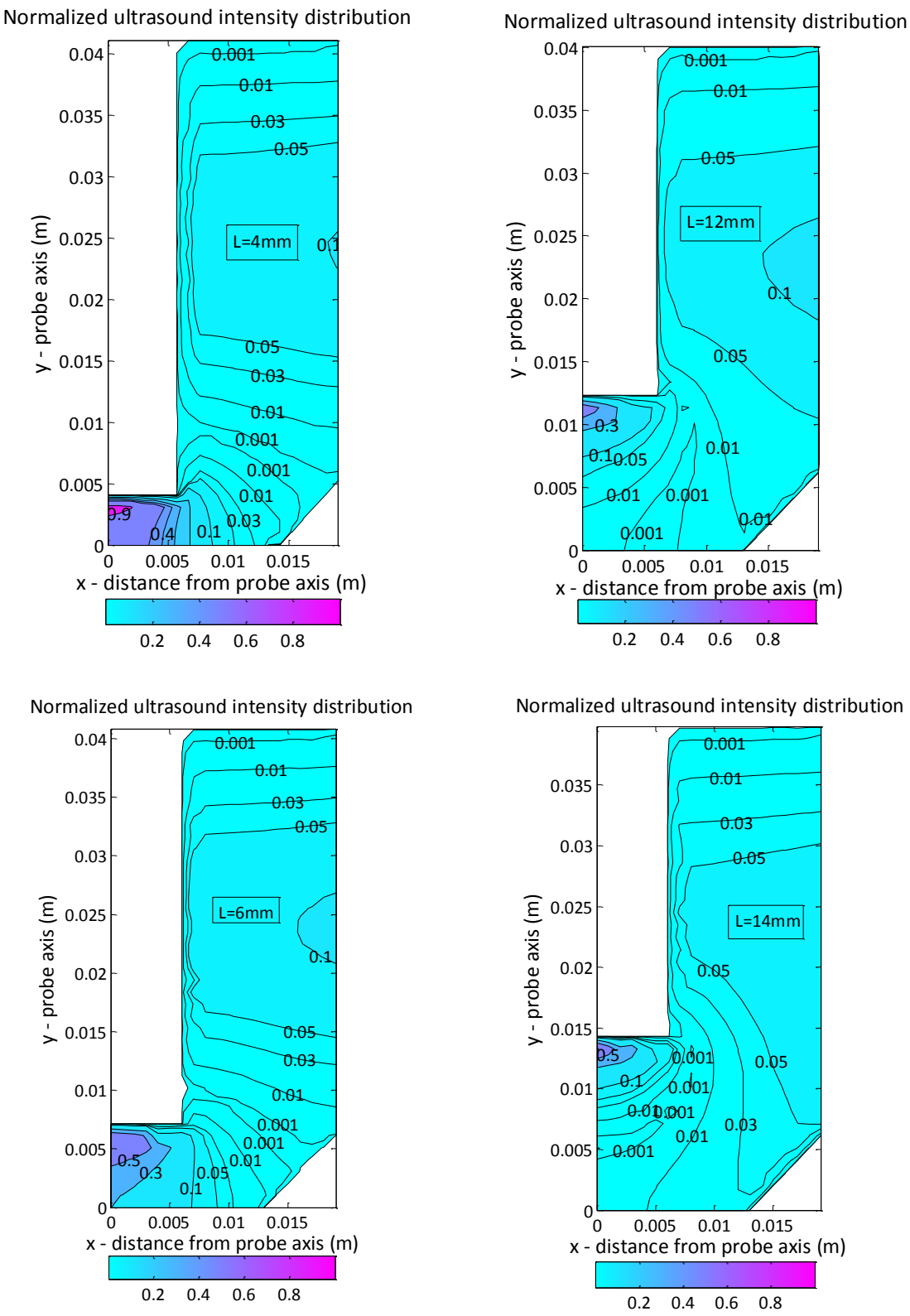

Figure A.2. Normalized ultrasound intensity distribution in the reactor

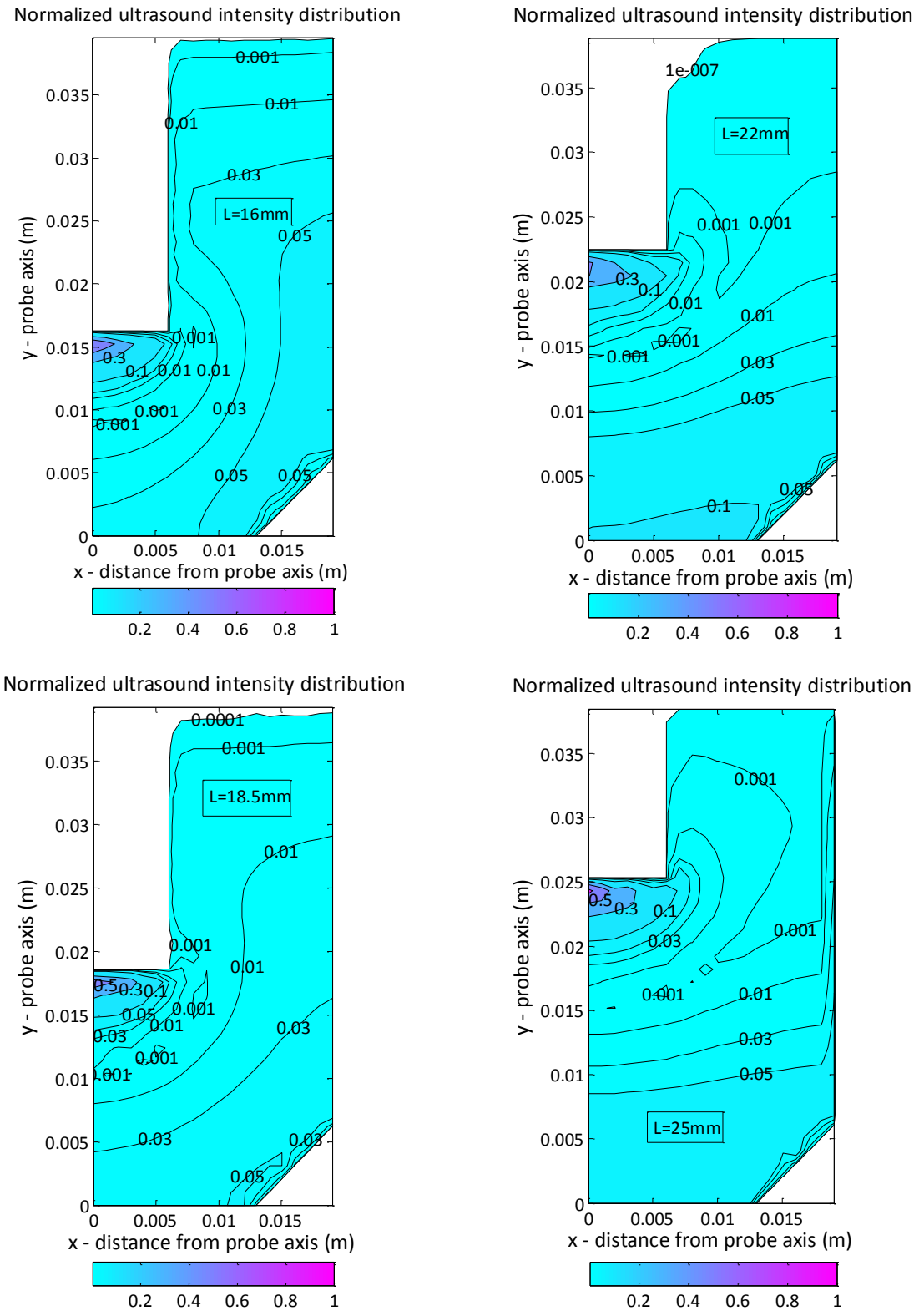

Figure A.2. Normalized ultrasound intensity distribution in the reactor (cont.)